DIPLOMARBEIT

Design and simulation of a solar tower cavity receiver with "solar salt" as heat transfer fluid

ausgeführt zum Zwecke der Erlangung des akademischen Grades eines Diplom-Ingenieurs

unter der Leitung von

Univ.Prof. Dipl.-Ing. Dr.techn. Markus Haider

E 302 - Institut für Energietechnik und Thermodynamik

eingereicht an der

Technischen Universität Wien

Fakultät für Maschinenwesen und Betriebswissenschaften

von

Lukas Panzer

0826395 (E 066 445)

Kreuzgasse 12

2551 Enzesfeld

Enzesfeld, August 2015

Kurzfassung

Dank der hervorragenden thermischen Speicherfähigkeit von Salzschmelzen, welche in thermischen Solarturmkraftwerken verwendet werden, wurde viel Aufwand betrieben um neue Receivergeometrien für diesen Kraftwerkstyp zu entwickeln. Ziel war es und ist es auch weiterhin, den Wirkungsgrad und das Betriebsverhalten der Receiver zu verbessern. Heutzutage gibt es zwei verschiedene Hauptvarianten von salzgefüllten Solarreceivern. Die erste Variante ist der sogenannte „External“ Receiver, welcher die solare Strahlung an der Oberfläche seiner Außenhülle (Rohrwand) aufnimmt. Im Gegensatz dazu nimmt der „Cavity“ Receiver die Sonnenenergie im Inneren eines windgeschützten Hohlraums bzw. einer Kavität auf. Diese Diplomarbeit beschäftigt sich mit der Auslegung und der Simulation eines salzgefüllten Cavity-Solarreceivers in einer neuartigen pentagonalen Bauform. Dazu wurden die Massenströme, die Temperaturen in den Rohrwänden und des Salzes und die Drücke im Zeitverlauf untersucht. Die äußeren Randbedingungen waren hierbei die solare Strahlung, die Windstärke am Receiver und die Umgebungstemperatur. Es wurden verschiedene Betriebszustände und Lastwechselvorgänge mit Hilfe der dynamischen Simulationssoftware Apros simuliert. Außerdem wurde eine Wärmeverlustberechnung für den Receiver durchgeführt und die Ergebnisse einer Spannungs- und Ermüdungsberechnung aus einer vorangegangenen Projektarbeit vorgestellt.

Abstract

Due to the thermal storability of solar salt, used in solar tower power plants, efforts have been made to develop new receiver geometries and to improve the overall performance of such power plants. There are two main configurations of molten salt receivers for solar towers. The first one, called external receiver, utilizes the outer shell as absorptive area, whereas the cavity receiver collects the energy of the sunlight, entering through a circular aperture on the inside. This thesis discusses the design and the simulation of a solar salt cavity receiver with a new pentagonal layout. The main aim was to examine the dynamic thermal behavior of the receiver and especially the molten salt. Therefore, the behavior of the mass fluxes, the temperatures in the pipe-walls and of the salt and the pressures over time was investigated for given solar radiation input, wind speed and ambient temperature. For the simulation of the operation a "hot-start" sequence, several "shutdown" sequences and a "whole-day" sequence were implemented using the dynamic Process Simulation Software Apros. Furthermore a heat loss calculation for the receiver and an evaluation of the thermal stresses of the receiver-pipes were performed.

Danksagung

An dieser Stelle möchte ich mich herzlich bei allen bedanken, die mich bei der Anfertigung dieser Arbeit unterstützt haben.

Zuerst möchte ich mich bei Herrn Professor Haider für die Betreuung bedanken und dass er es mir möglich gemacht hat, so ein interessantes Thema zu bearbeiten.

Mein besonderer Dank gilt auch Dominik Bothe und Gregor Klemencic, die in schwierigen Phasen der Arbeit an der Simulation sehr hilfsbereit waren und mir mit Rat zur Seite standen.

Weiters möchte ich Julian Apfelthaler für die Sprachkorrektur danken.

Zu guter Letzt bedanke ich mich herzlichst bei meiner Freundin Mercy und meinen Eltern Jochen und Gerlinde für die großartige Unterstützung während meiner Studienzeit.

Contents

1 Introduction **1**
- 1.1 Solar thermal electricity . . . 1
- 1.2 What has been done . . . 2
- 1.3 Solar irradiation . . . 3
- 1.4 CSP technologies . . . 3
- 1.5 Thermal storage . . . 5
- 1.6 Outlook . . . 5

2 Functional principle **6**
- 2.1 Simplified process scheme . . . 6
- 2.2 Receiver . . . 7

3 Stress and fatigue considerations **9**
- 3.1 Procedure . . . 9
- 3.2 Temperature distrubution . . . 9
- 3.3 Stress distribution . . . 11
- 3.4 Fatigue . . . 14

4 APROS simulation software **16**
- 4.1 General Configuration . . . 16
- 4.2 Thermal Hydraulics . . . 16
  - 4.2.1 Basic equations of the homogeneous model . . . 17
  - 4.2.2 Linearization and discretization for the homogeneous model . . . 18
  - 4.2.3 Solution procedure . . . 19
  - 4.2.4 Two phase model / 6 equation model . . . 20

5 Design of the cavity receiver **21**
- 5.1 Receiver- and other piping . . . 23
- 5.2 Design of the pumps . . . 24
- 5.3 Design of the salt tanks . . . 24
- 5.4 Summary of all dimensions . . . 25
- 5.5 Heat loss calculation . . . 26
  - 5.5.1 Properties of air . . . 27
  - 5.5.2 The emissive heat loss . . . 27

5.5.3 Reflective heat loss . . . 27
5.5.4 Convective heat loss - forced convection . . . 28
5.5.5 Convective heat loss - natural convection . . . 28
5.5.6 Conductive heat loss . . . 28
5.6 Discussion of the heat loss calculation . . . 29
5.7 Pressure loss of the receiver . . . 32
5.7.1 Tube friction . . . 32
5.7.2 Deflection, inlet and outlet losses . . . 32
5.7.3 Overall losses . . . 33

6 Apros model **34**
6.1 Material properties . . . 34
6.1.1 Solar Salt . . . 34
6.1.2 High nickel alloy steel . . . 35
6.2 Input data . . . 35
6.3 Process modeling . . . 37
6.3.1 Basic process . . . 37
6.3.2 Automation & control system . . . 39
6.4 Piping heat losses . . . 40
6.5 Restrictions . . . 41

7 Results **43**
7.1 Hotstart . . . 43
7.2 Shutdown - AP10 V5 M10 . . . 47
7.3 Shutdown - APopen V15 M10 . . . 51
7.4 Comparison of different shut downs . . . 54
7.5 Wholeday . . . 57

8 Conclusion **60**

A Apendix - process and automation diagrams **62**

1 Introduction

The trends in energy production at the present time are economically, environmentally and socially unsustainable. Without fast and strong action the emissions originating from common fossil fuel based energy generation would lead to significant global warming. Sustainable and low-carbon-emission energy technologies will play an essential role in the energy revolution, which is required to stop climate degradation. Solar thermal electricity (STE) produced by concentrating solar power (CSP) plants is one of those technologies. It has grown constantly over the past years, although less than expected by former prognoses. Meanwhile, the rapid growth of installed capacity and the decrease in costs of solar photovoltaics, as well as other important changes in the energy landscape, have led the International Energy Agency (IEA) to reassess the role of the distinct solar technologies regarding climate change. While the long term goal set for STE, which is reaching an 11% share of global electricity generation by 2050 remains unchanged, the medium-term prospects for STE deployment had to be corrected downwards. Even though PV has already established its position on the energy market, the STE technology will play an important role in long term, because of its built-in storage capabilities, that allow CSP plants to produce energy on demand. This advantage will even gain more importance as variable renewable energy sources, such as PV and wind power increase their shares of global electricity. One of the issues that slows down the propagation of this technology, is its capital intensity: almost all expenditures have to be made in advance. Lowering the cost of capital is a first important step for achieving the establishment of STE. Therefore clear and credible signals from politicians would lower risks and inspire confidence.

1.1 Solar thermal electricity

STE generates electricity without producing greenhouse gas emissions, so it can be a key technology for mitigating climate change. In addition, the flexibility of CSP plants regarding availability of the power helps to ensure energy security. In contrast to photovoltaic technologies, which directly generate electricity from solar radiation, CSP plants utilize steam turbines to harness the thermal power of the sunlight. They have also an inherent capability to store thermal energy for later conversion to electricity. Furthermore CSP plants can be equipped with backup heaters driven by fossil fuels. When combined

with thermal storage of several hours[1] capacity, CSP plants can produce electricity even when clouds block the sun or after sunset. Another advantage of STE is that the applied technologies in CSP plants have a potential for responding to specialized demands such as process heat for industry, co-generation of heating, cooling and power, and water desalination. They could also produce solar fuels which is an important area for further research and development.

1.2 What has been done

The STE industry has grown steadily since 2009 (Figure 1.1). This growth has been concentrated in Spain and the United States, but many other countries have also started projects. Market prices finally seem to be falling slowly. Thermal storage in molten salts is routinely used in trough configurations and has been used in demonstration solar towers. With 2304 MW of cumulative capacity (2014) Spain leads the world in STE, but will soon be overtaken by the United States. In Spain close to 2% of annual electricity are originated by CSP plants. The United States are in second place, with 900 MW at the end of 2013 and 750 MW added in 2014. Over 20 large projects are in early development, but not all will survive the permitting process. Other significant STE production in the rest of the world are in the United Arab Emirates and India, but also some CSP plants are in construction in Morocco and South Africa. A few smaller solar fields also exist in Algeria, Australia, Egypt, Italy, Iran and Morocco. Also China has announced very ambitious plans to install a capacity of up to 5000 MW in the next years.

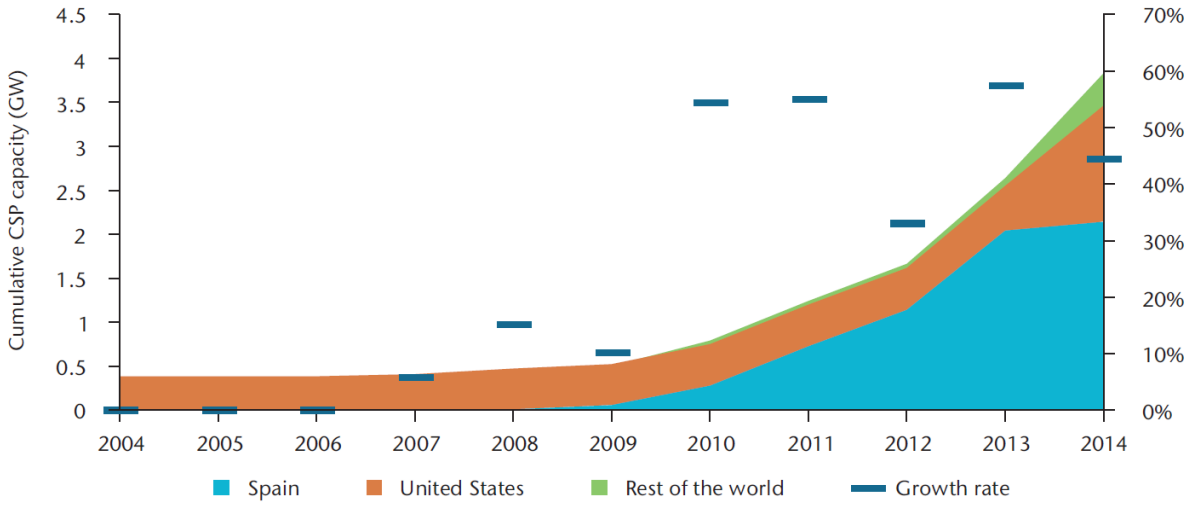

Figure 1.1: Devellopement of STE capacity [7]

[1] Term is explained in 1.5

1.3 Solar irradiation

Solar energy is the biggest energy resource on earth, with about 885 million TWh reaching the surface of the planet every year. The energy, reaching the surface corresponds to 1 $\frac{kW}{m^2}$ in clear conditions when the sun is near the zenith. It has two components: direct beam radiation straight form the sun and diffuse radiation, which comes indirectly after being scattered in all directions by the atmosphere. Direct normal irradiance (DNI) is measured on surfaces perpendicular to the direct sunbeam. Only DNI is relevant for devices that use lenses or mirrors to concentrate the radiation on smaller receiving surfaces. All places on earth receive sunlight half the of total hours of a year, but different areas receive different yearly average amounts of energy from the sun. When the sun is lower on the horizon, its energy is spread over a larger area. Furthermore, energy is lost by passing through the atmosphere, because of the increased (humid) air mass. The absorption characteristics of the atmosphere significantly affect the amount of received surface irradiation. In humid places, the atmosphere scatters the sun-rays and the DNI is lowered by the presence clouds and aerosols. The quality of DNI is essential for CSP plants, which is displayed by the fact that below a certain level of daily DNI, the net output of such a power plant is zero. High DNI is found in hot and dry regions with clear skies and low aerosol rate, which are typically in subtropical latitudes from 15° to 40° north or south. Closer to the equator the atmosphere is usually too humid and cloudy, especially during the monsoon season. At higher latitudes the climate also produce frequent cloudy conditions and the radiation must pass through more atmosphere mass to reach the power plant. DNI is also significantly higher at higher elevations, where absorption and scattering of sunlight due to aerosols is less. Therefore, the most favourable areas for CSP deployment are in North Africa, southern Africa, the Middle East, north-western India, the south-western United States, northern Mexico, Peru, Chile, the western parts of China and Australia. Other areas that are suitable include the very south of Europe and Turkey, other southern US locations, central Asian countries, places in Brazil and Argentina, and some parts of China

1.4 CSP technologies

CSP plants concentrate sunlight to heat a fluid, which directly or indirectly drives a steam turbine and in further consequence an electricity generator. This procedure allows to reach sufficient working temperatures of the fluid to ensure high efficiency in turning the heat into electricity, while limiting heat losses in the receiver. The three main CSP technologies are parabolic troughs (PT), linear Fresnel reflectors (LFR) and solar towers, also known as central receiver systems (CRS). Another type of CSP plant is a parabolic dish power plant. These types of power plants are different with respect to optical design, shape of receiver, nature of the transfer fluid and capability to store heat before it is turned into electricity Figure 1.2.

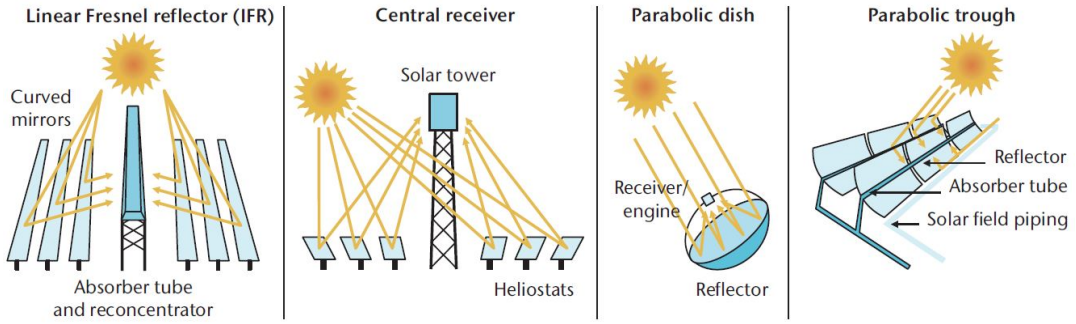

Figure 1.2: CSP technologies [7]

Parabolic trough Most installed capacities today are parabolic trough power plants which basically consist of long parabolic troughs, which track the sun on one axis. They concentrate the sunlight on linear receiver tubes isolated in an evacuated glass envelope. In these pipes oil[2] is heated up to 390°C, which transfers its heat to a conventional steam cycle.

Solar towers Central receiver systems (CRS), or solar towers have turned out as a viable alternative. One paramount example for this technology was built by BrightSource at Ivanpah in California, with a total net capacity of 377 MW el, which is the largest installed CSP capacity so far at a single site. The plant gathers three distinct receiver towers based on direct steam generation technology with one turbine for each tower and no storage. The tower technology is the second best choice with respect to concentration ratio and theoretical efficiency after parabolic dishes, and offers the largest prospects for future cost reductions. The functional principle is described in more detailed in chapter 2.

Linear Fresnel receivers LFR approximate the parabolic shape of trough systems but use long rows of flat or slightly curved mirrors to reflect the radiation of the sun onto a downward-facing linear, fixed receiver. LFR are relatively compact and their almost flat mirrors are easier to manufacture than parabolic troughs. The mirror aperture can be augmented more easily than with troughs and secondary reflection provides higher possible concentration factors, reducing thermal losses. The disadvantage of the LFR are the higher optical losses compared to parabolic trough power plants when the sun is low on the horizon. This reduces the electricity generation in in the morning and the evening, but also during winter.

Parabolic dishes Parabolic dishes, which are supporting individual heat-to-electricity engines [3] at their focus points and have almost disappeared from the commercial energy portfolio. Despite having the best optical efficiency, it was not possible to reduce the higher costs and risks of the technology. In addition thermal storage is difficult.

[2]Direct steam configuration with water/steam as heat-transfer-fluid is content of new research.
[3]Stirling motors

1.5 Thermal storage

In addition to the short term buffering capabilities that every CSP power plant has, a few years ago operators started to use thermal storage systems. These facilities store sensible heat utilizing a mixture of molten salts. During the day, excess heat is diverted to a storage material (e.g. molten salts). If electricity production is required after sunset, the stored heat is used for the steam cycle. Storage size is defined as the number of hours the plant can run at rated capacity on stored heat only. The optimal size of storage depends on the purpose of it. Small thermal storage avoid losses of energy that would arise on the most sunny hours or days from waste of excess heat. Under similar sunshine conditions, larger solar fields and storage capabilities for a given turbine size could be used to receive a greater annual electrical output. On the other side, for a given solar field the storage size and the turbine size can be adjusted for different purposes. For example shifting or extending generation by a few hours to cover evening peaks, when the economic value of electricity is higher, or even generating round the clock part of the year to cover base load. The rapid cost reduction of PV systems seems to have made CSP without storage almost irrelevant. The increased share of PV in the energy mix will increase the need for flexible, fast controllable technologies. CSP plants with five to ten hours of storage capacity will be well-suited for this challenge. Thermal storage also has very high efficiency, especially if the storage medium is also used as heat transfer fluid. A return efficiency of about 98% is possible.

1.6 Outlook

It is expected by the IEA that STE becomes competitive on more markets and its deployment will grow faster after 2020. The rapid deployment of PV has delayed the deployment of STE by now but in long term the STE will establish because of its storage opportunity. This feature is a strong advantage for operating a power plant and could be also used to compensate power fluctuations of other sources with varying energy output (wind and photovoltaic). Many countries are only just beginning to develop CSP plants. Unfortunately also stagnation of development under some circumstances is possible for some time periods. For example there are STE projects in Spain stopped recently for a while because of incentives that have been cut. Nevertheless Spain has, as many other developed countries a national action plan, which provides for the reach of an ambitious goal of capacity. Each country will have to choose which actions to prioritize and on which technology they want to bet to reach their aims. Considering all influencing factors named in this section, the IEA made a long-term forecast were STE is expected to represent about 11% of total electricity generation by 2050.

All the information and graphs of the previous chapter are taken from [7] unless otherwise indicated.

2 Functional principle of a solar cavity receiver

The solar tower with molten salt as heat transfer fluid and 5 to 10 hours storage decouples the availability of solar energy from the electric grid demand. This feature makes it a very promising technology for today's and tomorrow's energy supply. The power plant is divided in five major sections: the heliostat mirror field, the molten salt central receiver (MSCR), the thermal energy storage (TES), steam generator (SG) and power block. The simplified functional principle of the molten salt solar tower is described in this section.

2.1 Simplified process scheme

In Figure 2.1 one can see how the heliostat mirror field (1) is focusing the sun beams on the receiver (3) on the top of the tower. The salt is transferred from the cold salt storage tank (2) to the hot salt storage tank (4) through the MSCR. The receiver works as a heat exchanger, which is harnessing the solar radiation to heat up the salt from about 285°C to 560°C. The salt, with the temperature of 560°C is stored in the hot salt storage tank, of which the required amount of salt is pumped through the steam generation system to the cold salt storage. The steam generation system consists of the heat exchanger (5), which absorbs the heat of the salt to produce steam, the steam turbine (6), which transfers the thermal energy into mechanical power, and the generator (7), which finally delivers the electricity to the transformer (8). The operator pumps just the amount of salt through the steam generation system that is needed to satisfy the electricity demand of the grid. The hot salt tank works as a buffer that takes up energy if the available solar energy is higher than the demand and delivers energy if it is other way round. In the publication [10] it is stated that the use of molten salt directly as heat transfer fluid (HTF) in the solar receiver, eliminates the inefficiency, that occurs, if the molten salt is heated indirectly for thermal storage. This direct storage opportunity is a significant advantage to steam or another HTF. To be specific, the direct steam solar power plant is using water/steam as the HTF to collect and transport the energy, received from the solar irradiation, to the steam turbine for power generation. Excess energy obtained from the solar field in the direct steam central receiver (DSCR) can be stored in the TES using a steam to salt heat exchanger. Therefore the energy stored in the storage system can be used used to generate power on demand. The additional heat exchanger in the

direct steam solar plant is responsible for extra energy losses, which do not appear in the molten salt solar power plant. Other advantages of the MSCR system design include the optimized start-up and shut-down operation, robust response for cloud events [1], and design for optimal efficiency.

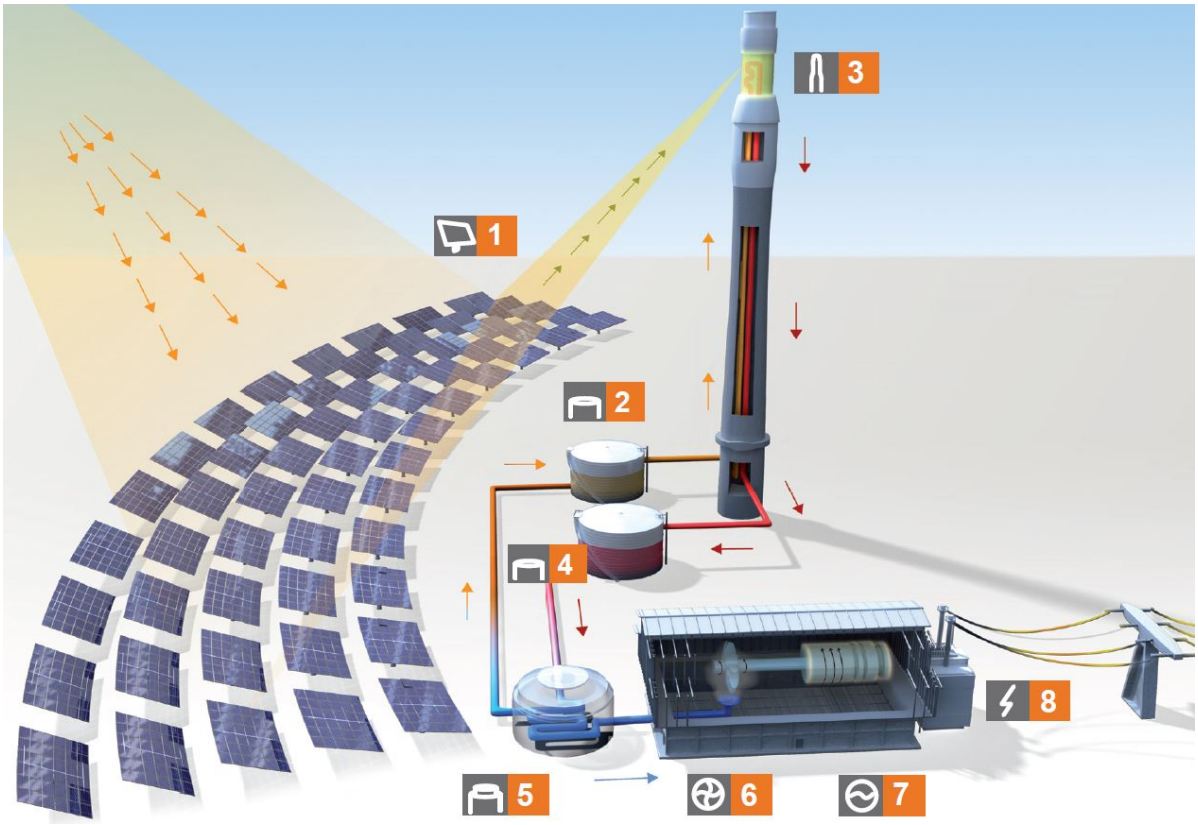

Figure 2.1: Solar power tower process flow scheme - (1): Heliostat mirror field; (2): Cold salt storage tank; (3): Receiver; (4): Hot salt storage tank; (5): Heat exchanger; (6): Steam turbine; (7): Generator; (8): Transformator (source: [2])

2.2 Receiver

In the current section the process of the salt in the receiver is described based on reference [10] unless otherwise indicated.
The molten salt central receiver can be seen as interface between the solar field and the molten salt. It is attached to the top of the structural tower, positioned in the focal point of the mirror field. The salt is pumped from the cold salt storage tank through

[1] Annotation: The advantage of the molten salt compared to the direct steam configuration in operation is that no phase change occurs. Therefore the pressure level is much lower (∼130 bar for direct steam [19] vs. ∼ 3 bar in molten salt receiver (chapter 7) and the pressure variations should pose no stability problems for the pipes.

the supply pipe to the inlet vessel. This vessel provides the required pressure to secure uninterrupted flow through the receiver. It also keeps a minimum amount of salt available all the time to support proper shutdown during an unexpected event, for example if the supply pump is breaking down. For that purpose a pressurized air pillow is obtained by an air compressor over the salt phase, which provides stable inlet conditions at the control valves that control the flow through the receiver. In case of an emergency shut down, the salt of the inlet vessel is forced to maintain the flow through the receiver for at least 60 seconds ([23]) to allow the mirror field to defocus and to prevent critically high pipe or salt temperatures. In normal operation the salt flows from the inlet vessel through a series of tube panels arranged in passes. Each panel is composed of high nickel alloy pipes ([23]), which are comprising the heat transfer surface tubes and are reaching from an inlet header to an outlet header. Multiple panels comprise one single pass and the MSCR has several passes, which are organized in serpentine flow arrangement. This means that the flow changes its direction in the vertical orientation, as salt is discharged from one pass to the next. The the overall mass flow is split up into two separate parallel flow paths called branches. The two branches each comprise one half of the of the MSCR. Each flow path has its own flow control (control valve 1 and control valve 2 [2]) to adjust the optimal mass flux for each path separately (east side path and west side path). The two branches lead the salt into the outlet vessel. This vessel acts as a buffer between the receiver and the hot salt tank of the TES. The outlet vessel is sized to accept a certain amount of salt from the receiver during an unexpected event, for example in case of a blocked down-comer pipe. The hot salt return pipe, or down-comer pipe respectively leads the high temperature salt from the outlet vessel to the hot salt storage tank of the TES.

All the information of the previous chapter is taken from [10] unless otherwise indicated.

[2]See also process diagram - Figure A.2

3 Stress and fatigue considerations of receiver pipe-walls for receiver design

Due to the high occurring temperatures and the frequent load changes in a molten salt solar tower receiver, the pipe material has to be very resilient. When a receiver is designed, one has to prove first that the pipe walls bear the load. If this requirement is not fulfilled, the walls have to be made thicker or the operation mode has to be changed. In this section the results of temperature- and stress-field and fatigue calculations for a receiver pipe are presented. This chapter summarizes the preliminary project work of [17], which is highly merged to this diploma thesis.

3.1 Procedure

To validate that the receiver-pipes remain undamaged for the whole lifespan, a fatigue calculation was performed. Therefore the previous calculation of the stress distribution and in further consequence the temperature distribution is required. The dimensions of the pipes of the pipe-walls are: outer diameter $d_a = 25\ mm$; inner diameter $d_i = 20\ mm$; pitch $t = 35\ mm$[1]. The thermal capacity of the whole system is assumed with 8 MW. The maximum heat-flux-density is chosen with $q_a = 500\ \frac{MW}{m^2}$ depending on the available radiation. The average salt temperature Θ_m at the inlet of the receiver shall be 285 °C and 560 °C at the outlet. The mass-flux-density (MFD) of the salt is ranged between 700 and 3000 $\frac{kg}{s}$ to ensure the sufficient cooling of the pipe-walls.

3.2 Temperature distrubution

Membrane pipe-walls To calculate the temperature field in membrane walls with finned tubes, diagrams from IET [4]were used. To be specific, the temperatures at certain points of the pipe wall profile can be calculated. The disadvantage of these diagrams

[1]The values of these properties are not the same as the ones used for the dynamic receiver simulation (chapter 5)! The reason for this is, that the temperature field of the membrane wall in this chapter is based on the diagrams of [4] which only provide certain fixed dimensions of the pipes

is, that they are only valid for certain pipe dimensions and for constant and evenly distributed radiation to one side of the pipe wall.

Single-pipe-walls To calculate the temperature field in single-pipe-walls the publication „Theoretische Untersuchung der Temperaturverteilung in strahlungsbeheizten Kesselrohren“ [18] was used. The formulas of this document, which were developed for a combustion chamber, were adapted for the needs of the receiver and simplified. In the following diagrams the results of the temperature field calculations are illustrated for one pipe of a membrane-wall (Figure 3.2) and a single-pipe-wall (Figure 3.1) respectively. The x-axis trough the center of the pipe shows in direction of the incident radiation for all diagrams of this chapter. One can see that the temperature in the finned tube is distributed more homogeneously than in the single pipe. The reason for this is probably, that additional heat is led from the fin to the pipe itself. As expected the hottest point is on the front side in direction of the arriving heat flux.

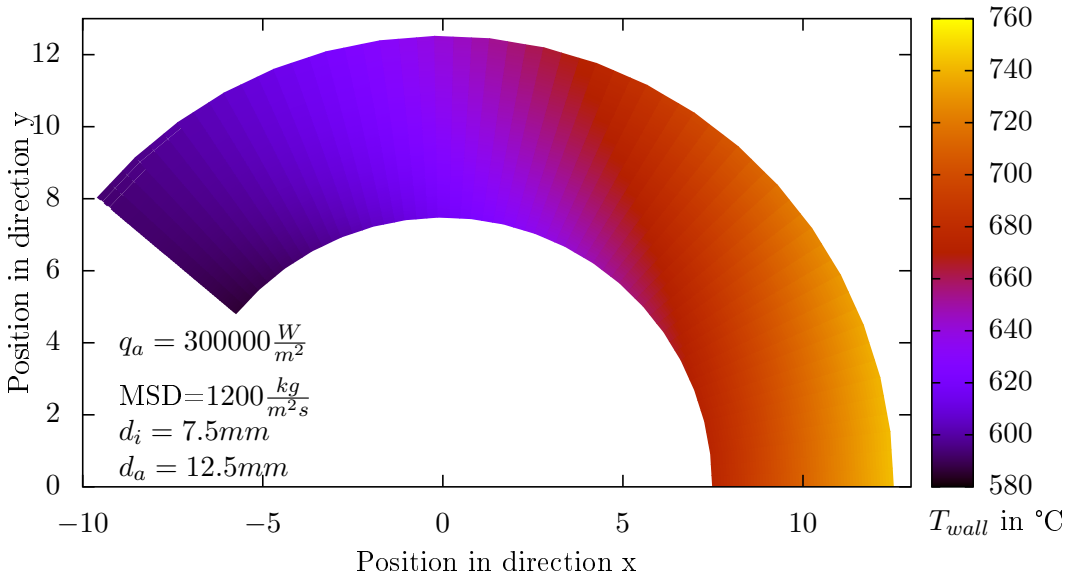

Figure 3.1: Temperature distribution for $\Theta_m = 560$ °C - single

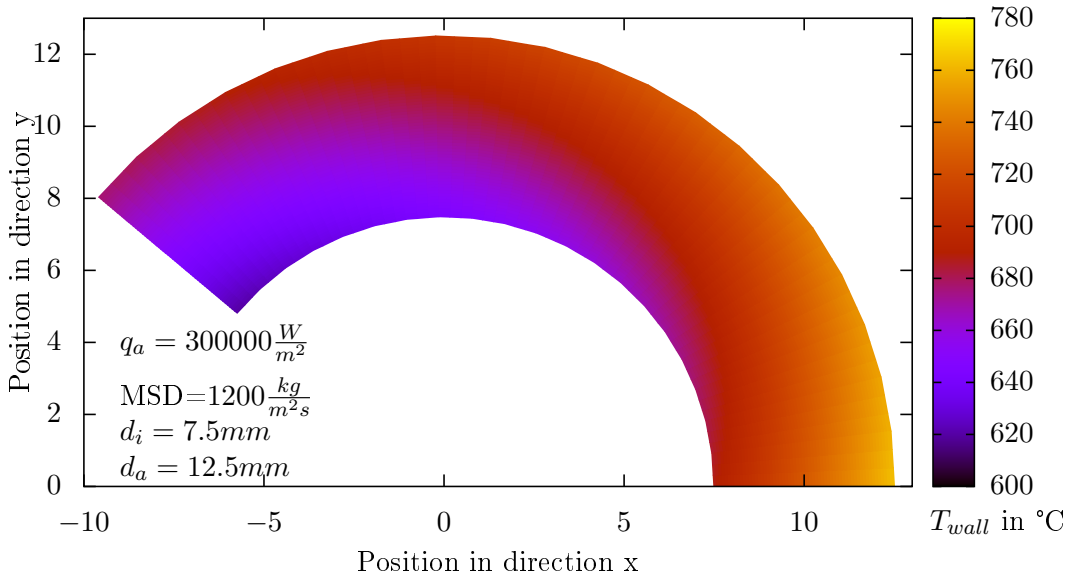

Figure 3.2: Temperature distribution for $\Theta_m = 560$ °C - membrane

3.3 Stress distribution

To receive the stress field, the analytic formulas for calculating thermal stress in thick hollow cylinders of [12] were used. In the following diagrams the results of the radial or tangential stress distribution calculations are illustrated for one pipe of a membrane-wall (Figure 3.4;Figure 3.6) and a single-pipe-wall (Figure 3.3; Figure 3.5) . Similar to the temperature field, one can see that stress is distributed more equally in membrane walls than in single-pipe-walls. This is reasoned by the fact that only the thermal stresses are considered and they are mainly dependent of temperature differences. Furthermore the maximum stress values are higher in the membrane walls and the range of the tangential stress is one order of magnitude higher than the range of the radial stress. The highest absolute value of stress occurs on the front side of the pipe at the inner radius in tangential direction in both the finned tube and the single-pipe.

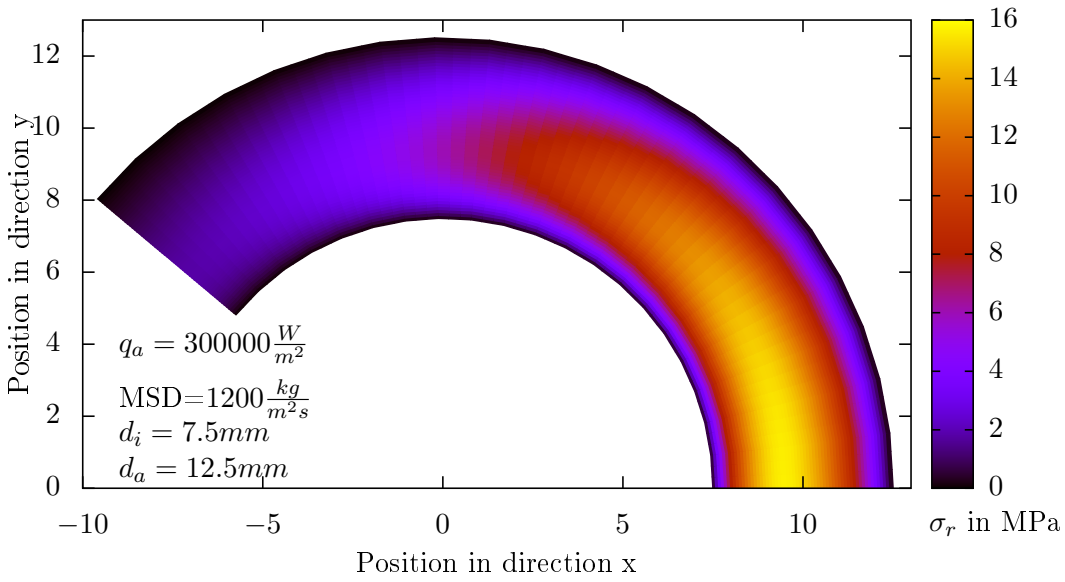

Figure 3.3: Radial stress for $\Theta_m = 560$ °C- single

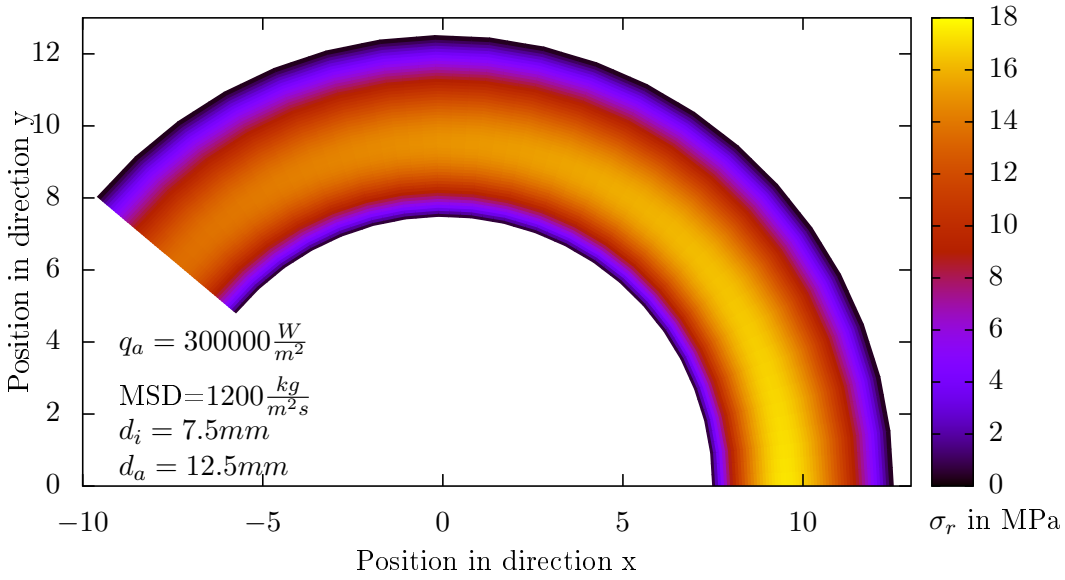

Figure 3.4: Radial stress for $\Theta_m = 560$ °C- membrane

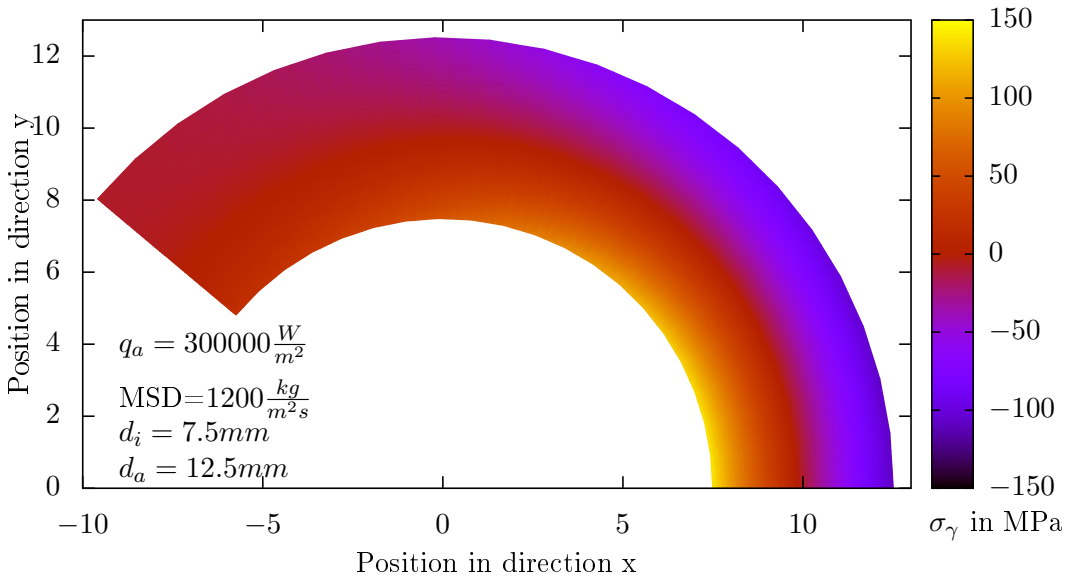

Figure 3.5: Tangential stress for $\Theta_m = 560$ °C- single

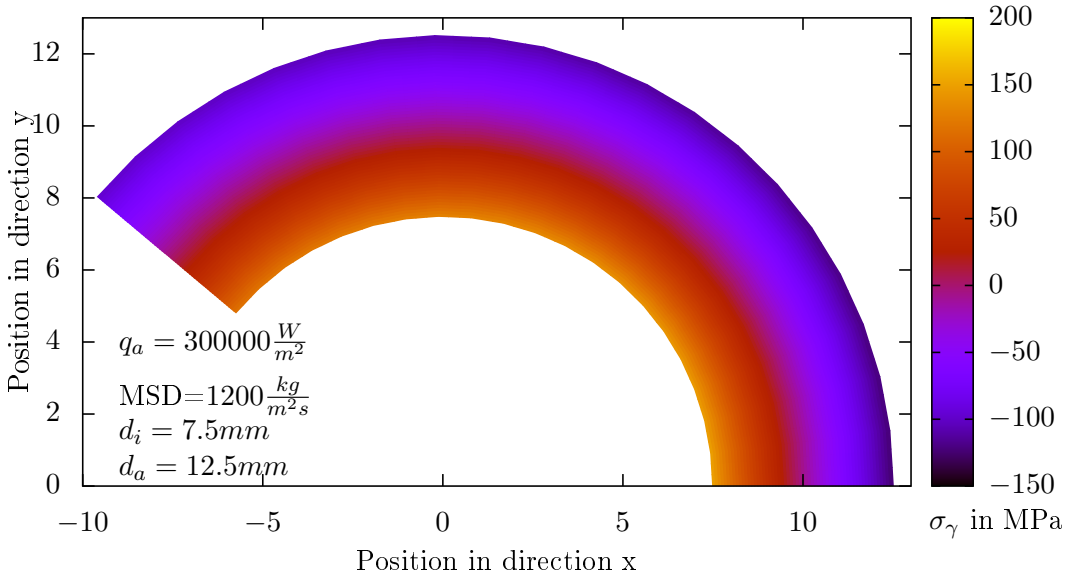

Figure 3.6: Tangential stress for $\Theta_m = 560$ °C - membrane

3.4 Fatigue

To prove that the pipe-wall resists the load change, a fatigue calculation was realized for the highest stressed points of the pipe-wall cross section with the help of the DIN norm 1295-3 [6]. It was assumed that the pipe-walls have to bear 15800 cycles-to-failure. The results of the fatigue calculation (shown in Table 3.1) are influenced mainly by the parameters mass-flux-density and heat-flux-density. A high heat-flux-density will lead to higher temperature differences in the pipe, whereas the higher mass-flux-density will lead to lower temperatures in the whole wall of the tubes due to being cooled by the salt flow [2]. Also the the stress values are higher for higher MFD. The reason for this behavior are the lower temperatures that occur in the pipe, which decrease the ability of the steel to conduct heat. As a result, the temperature difference becomes bigger, if the heat flux is held constant. This correlation is illustrated in (3.1) given in [11] and through the curve of the thermal conductivity λ (Figure 3.7) of the pipe material (steel). In this formula $\dot{q}$ is the heat-flux-density, s is the thickness of the pipe wall, Φ is a constant correction factor (for given dimensions) and ΔT is the difference of the temperatures at the inner and the outer surface. Table 3.1 shows that one has to be careful, as with some combinations of these parameters the "relevant stress range" exceeds the "permissible stress range". Following the abbreviation of the source [6], the indices L mean "Lastspielsicherheit" which could be translated with load-cycle-safety and indices S mean "Spannungssicherheit" which could be translated with stress-safety. As one can easily verify with Table 3.1, the permissible stress range for load-cycle-safety is more strict than regarding stress-safety.

$$\frac{\dot{q} \cdot s}{\lambda} = \frac{\Delta T}{\Phi} \tag{3.1}$$

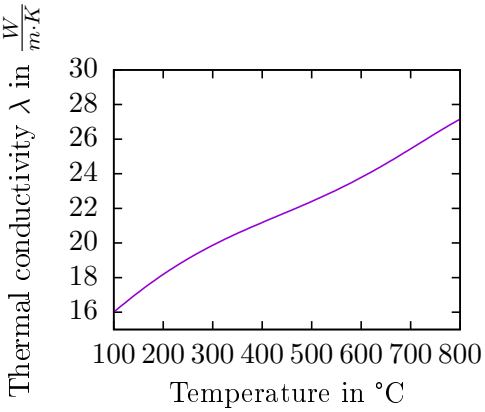

Figure 3.7: Thermal conductivity of the steel (See also 6.1.2) in dependence of the temperature. To receive the λ, needed in equation (3.1), one has to insert the average temperature of the pipe-wall.

[2] In normal operation of the receiver, the temperatures at the outer surface of the pipes are higher than the temperature of the salt Θ_m. Therefore the salt is cooling the inner surface of the wall.

Table 3.1: Fatigue calculation results

MFD in $\frac{kg}{m^2 s}$	q_a in $\frac{kW}{m^2}$	single-pipe/ finned tube	permissible stress range	relevant stress range
2000	500	SP	σ_{p_L}=615.647 MPa σ_{p_S}=1240.636 MPa	σ_{rel_L}= 703.802 MPa σ_{rel_S}= 596.931 MPa
2000	300	SP		σ_{rel_L}= 273.953 MPa σ_{rel_S}= 250.861 MPa
1200	300	SP		σ_{rel_L}= 262.193 MPa σ_{rel_S}= 241.877 MPa
1200	300	FT		σ_{rel_L}= 283.182 MPa σ_{rel_S}= 261.029 MPa
1200	500	FT		σ_{rel_L}= 778.966 MPa σ_{rel_S}= 660.681 MPa

The conclusion of this chapter is that the results of the calculation are plausible. Therefore the aim of proving the suitability of the receiver pipes can viewed as fulfilled by the illustrated results. However, the underlying calculations are only the first step to further research on this topic, because many simplifications had to be made to keep the effort in reasonable scope. The analytic formulas that are used only consider the stresses due to temperature differences. However, the attachment of the pipes in a real configuration were not considered, even-tough the influence of mounting is expected to be significant. A finite elements software is recommended for further research on this topic, to improve the accuracy of the calculation and to find more results with an acceptable investment of time.

4 Description of the APROS simulation software

APROS (Advanced PROcess Simulator) is a process simulation software developed by VTT Technical Research Centre of Finland and Fortum, which is able to simulate thermal hydraulic processes in power plants dynamically. In this chapter, based on [19], the theoretical background of this powerful but tricky dynamic simulation tool is introduced.

4.1 General Configuration

APROS consists of three subsystems, which are described below, according to [21].

- **GUI** - Graphical User Interface: The user can control APROS either by configuring the model in the graphical user interface or directly by giving commands in the command window. The various modules are chosen of the model menu and are set by drag and drop in the diagram editor. As a result, a flow sheet is created. The properties of the different modules can be changed by opening the property view and clicking on the model that should be configured.
- **OPC** - The process control is used for the simulation of the automation system.
- **APROS** - The calculation algorithm itself solves the conservation as well as the constitutive equations and contains the solution method. The simulation software can be controlled directly via a command window.

4.2 Thermal Hydraulics

With the APROS process simulation software, the multi-component flow can be simulated with different resolutions. A homogeneous model and 2 heterogeneous models (5-equation and 6-equation multi-fluid models) are available. Since the liquid module "OIL" has just the homogeneous model as option, this 3-equation solution method was used for the whole simulation of the system and is described in the next two sections.

4.2.1 Basic equations of the homogeneous model

The dynamic conservation equations for mass (4.1), momentum (4.2) and energy balance (4.3), which have to be solved simultaneously for the entire model network, are given below.

$$\frac{\partial A\rho}{\partial t} + \frac{\partial A\rho v}{\partial z} = 0 \tag{4.1}$$

$$\frac{\partial A\rho v}{\partial t} + \frac{\partial A\rho v^2}{\partial z} = S - A\frac{\partial p}{\partial z} \tag{4.2}$$

$$\frac{\partial A\rho h}{\partial t} + \frac{\partial A\rho v h}{\partial z} = S \tag{4.3}$$

The flow area A, the density ρ, the flow velocity v, the pressure p and the enthalpy h are the variables. The source-terms S can be used to describe feed effects (sources or sinks) that cannot be described with the basic equations only. For example heat transfer between the fluid and the pipe walls or friction between two phases (6-equation model) can be considered in the equation with source terms. To solve these partial differential equations, discretization and linearization of the non linear terms has to be performed. For the spatial discretization staggered grids are used where mass or energy and momentum control volumes are not the same, as illustrated in Figure 4.1. These volumes have a so called "node" in the center and are connected by “branches” like indicated in Figure 4.2, where k,i, and j are the nodes and ki and kj respectively are the branches.

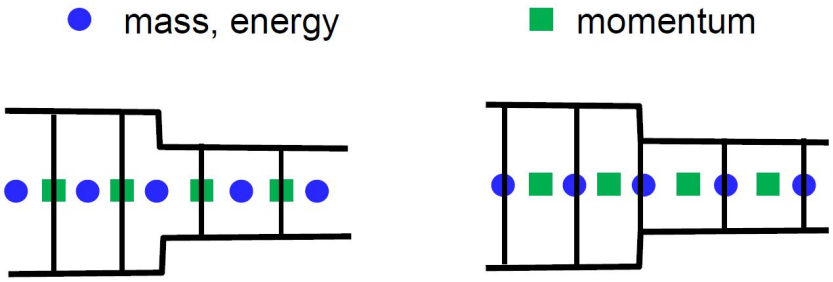

Figure 4.1: Control volumes for mass/energy or momentum [13]

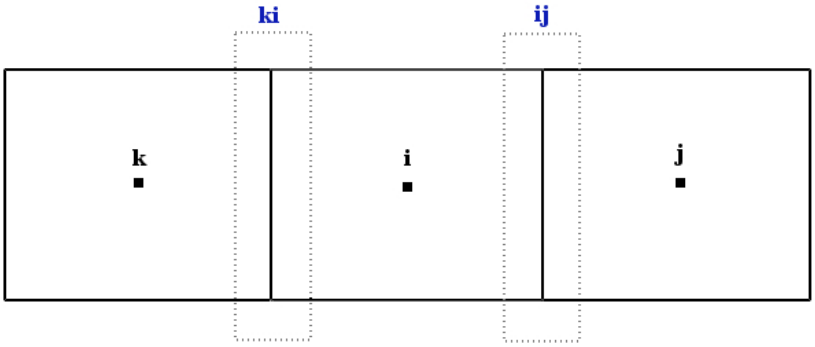

Figure 4.2: Scetch of nodes and branches

4.2.2 Linearization and discretization for the homogeneous model

Mass equation The mass equation (4.1) is linearized and discretized with the transformations $\partial t \Rightarrow \Delta t$ and $\partial z \Rightarrow \Delta z$ and multiplied by Δz, which leads to the following expression:

$$\frac{V_i}{\Delta t}\left(\rho_i^n - \rho_i^{t-\Delta t}\right) = -\sum_{i \neq j} \dot{m}_{ij}^n \tag{4.4}$$

Where the node Volume $V_i = A_i \Delta z$ and the mass flow $\dot{m}_{i,j}^n = A_{ij}\rho_{ij}v_{ij}$ from the node i to j are used. With the help of the Taylor formula (4.5) the new density (superscript n) at node is linearized around the density at the previous time-step (superscript o). Multiple iterations have to be made every time step to approximate the new properties.

$$\rho_i^n = \rho_i^o + \frac{\partial \rho_i^o}{\partial p_i^o}\left(p_i^n - p_i^o\right) \tag{4.5}$$

The new density in equation (4.4) is replaced by formula (4.5) and results in the discretized mass equation:

$$\frac{V_i}{\Delta t}\left(\rho_i^o - \rho_i^{t-\Delta t}\right) + \frac{V_i}{\Delta t}\frac{\partial \rho_i^o}{\partial p_i^o}\left(p_i^n - p_i^o\right) = -\sum_{i \neq j} \dot{m}_{ij}^n \tag{4.6}$$

Momentum equation With the same approach one can calculate the discretized energy equation:

$$\frac{\Delta z_{ij}}{A_{ij}}\left(\frac{\dot{m}_{ij}^n - \dot{m}_{ij}^{t-\Delta t}}{\Delta t}\right) - p_i^n + p_j^n + \frac{1}{2}K_{ij}\dot{m}_{ij}^{n^2} + \frac{\left(\dot{m}_{ij}^n\right)^2}{\rho_{ij}Aij^2} - \frac{\dot{m}_{ki}^2}{\rho_{ki}A_{ki}A_{ij}} = S_i \tag{4.7}$$

Where the equations (4.8), (4.9) and (4.10) are used to abbreviate some terms in (4.7):

$$\Delta p^n = \frac{1}{2}\rho_{ij}\varsigma_{ij}v_{ij}^2 \tag{4.8}$$

$$K_{ij} = \frac{\varsigma_{ij}}{\rho_{ij} A_{ij}^2} \tag{4.9}$$

$$\Delta p^n = \frac{1}{2} K_{ij} \dot{m}_{ij}^{n^2} \tag{4.10}$$

Furthermore the pressure loss Δp^n with the pressure loss coefficient ς can be linearized with the Taylor polynomial (4.11):

$$\Delta p^n = \frac{1}{2} K_{ij} \left(\dot{m}_{ij}^o\right)^2 + \frac{\partial \Delta p^o}{\partial \dot{m}_{ij}^o} \left(m_{ij}^n - \dot{m}_{ij}^o\right) = K_{ij} \dot{m}_{ij}^o \dot{m}_{ij}^n - \frac{1}{2} K_{ij} \left(\dot{m}_{ij}^o\right)^2 \tag{4.11}$$

With the pressure loss (4.12) of the previous time step:

$$\Delta p^o = \frac{1}{2} K_{ij} \left(\dot{m}_{ij}^o\right)^2 \tag{4.12}$$

If the equation (4.11) is inserted in formula (4.7), the following expression (4.13) is produced.

$$\frac{\Delta z_{ij}}{A_{ij}} \left(\frac{\dot{m}_{ij}^n - \dot{m}_{ij}^{t-\Delta t}}{\Delta t} \right) - p_i^n + p_j^n + K_{ij} \dot{m}_{ij}^o \dot{m}_{ij}^n - \frac{1}{2} K_{ij} \left(\dot{m}_{ij}^o\right)^2 + \frac{\left(\dot{m}_{ij}^n\right)^2}{\rho_{ij} A i j^2} - \frac{\dot{m}_{ki}^2}{\rho_{ki} A_{ki} A_{ij}} = S_i \tag{4.13}$$

The term $\frac{\left(\dot{m}_{ij}^n\right)^2}{\rho_{ij} A i j^2}$ has to be linearized accordingly.

Energy equation With the same approach one can calculate the discretized energy equation, using again the the node volume $V_i = A_i \Delta z$ and the mass flow $\dot{m}_{i,j} = A_{ij} \rho_{ij} v_{ij}$ from the node i to j, inserted in (4.3):

$$V_i \left(\frac{\rho_i^n h_i^n - \rho_i^{t-\Delta t} h_i^{t-\Delta t}}{\Delta t} \right) - \sum_{in} \dot{m}_{ij}^n h_{ij}^n + \sum_{out} \dot{m}_{ij}^n h_{ij}^n = S_i \tag{4.14}$$

4.2.3 Solution procedure

The discretized and linearized mass, momentum and energy balance equations for every node provide a linear equation system which can be solved step by step as described hereafter (following the argumentation of [13]):

1. $\dot{m}_{ij}$ is calculated with the momentum equation (4.13) and inserted in the mass equation
2. A system of algebraic linear equations dependent of the pressures is received
3. The pressures are solved using matrix calculation methods
4. All mass flows are calculated from the corresponding new pressures

5. The obtained values of the mass flows are inserted in the energy equation
6. The system of linear equations for enthalpies is solved
7. The Material properties in dependence of pressure p and enthalpy h are updated
8. Iteration until the desired accuracy is reached

4.2.4 Two phase model / 6 equation model

To simulate two phase flows, the conservation correlations for mass, momentum and energy have to be calculated for each phase separately. Thus, six equations are obtained:

$$\frac{\partial(\alpha_k \rho_k)}{\partial t} + \frac{\partial(\alpha_k \rho_k v_k)}{\partial z} = \Gamma_k \tag{4.15}$$

$$\frac{\partial(\alpha_k \rho_k v_k)}{\partial t} + \frac{\partial(\alpha_k \rho_k v_k^2)}{\partial z} + \alpha_k \frac{\partial p}{\partial z} = \Gamma_k v_k + \alpha_k \rho_{ik} \bar{g} + F_{ik} + F_{va} + F_{fl} + \Delta p_{pu} \tag{4.16}$$

$$\frac{\partial(\alpha_k \rho_k h_k)}{\partial t} + \frac{\partial(\alpha_k \rho_k v_k h_k)}{\partial z} = \alpha_k \frac{\partial p}{\partial t} + \Gamma_k h_{ik} + q_{ik} + q_{wk} + F_{ik} v_{ik} \tag{4.17}$$

By inserting either liquid or gaseous for the index k, that represents the phase, 6 equations are received out of the 3 formulas listed above (4.15)(4.16)(4.17). The indices i and w stand for interface between phases respectively the pipe wall. α is the volume fraction of the phase, Γ the mass transfer between the phases, q the heat transfer and $\bar{g}$ the gravitational constant. $F_{ik,wk,va,fl}$ characterize the friction between two phases, between a phase and the wall, generated by a valve and due to a change of geometry. Δp_{pu} is the pressure loss of a pump.

All the information of the previous chapter is taken from [19] unless otherwise indicated.

5 Design of the cavity receiver

The design of the receiver is based on the preliminary works of [19] and [23] The dimensions of the walls, which are forming the outer shell of the cavity, are shown in picture 5.1. The height of the receiver is 4.2 m. The cavity has an aperture with a diameter of 3 m in the bottom wall, where the concentrated sunlight is entering. It can be closed by an aperture-door within 10-60 seconds. The solar salt, consisting of 60 % of $NaNO_3$ and 40 % of KNO_3, flows through the receiver in 2 flow-paths and is heated up from 285 °C to about 560 °C in normal operation. The cavity is located between an inlet and an outlet tank. The inlet tank provides a pressure of 3 bar to assure steady flow through the receiver-tubes, which is produced by a compressed air supply. The receiver is designed for a nominal thermal capacity of 8.5 MW.

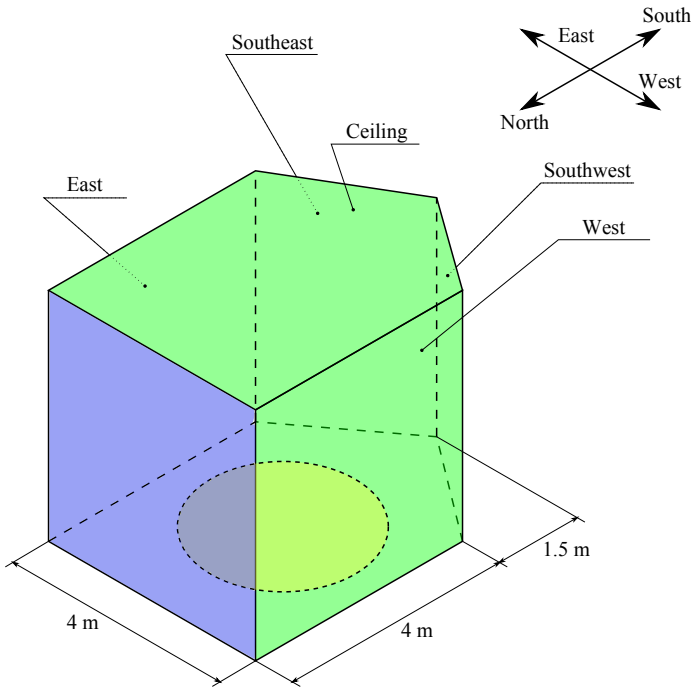

Figure 5.1: Receiver dimensions [3]

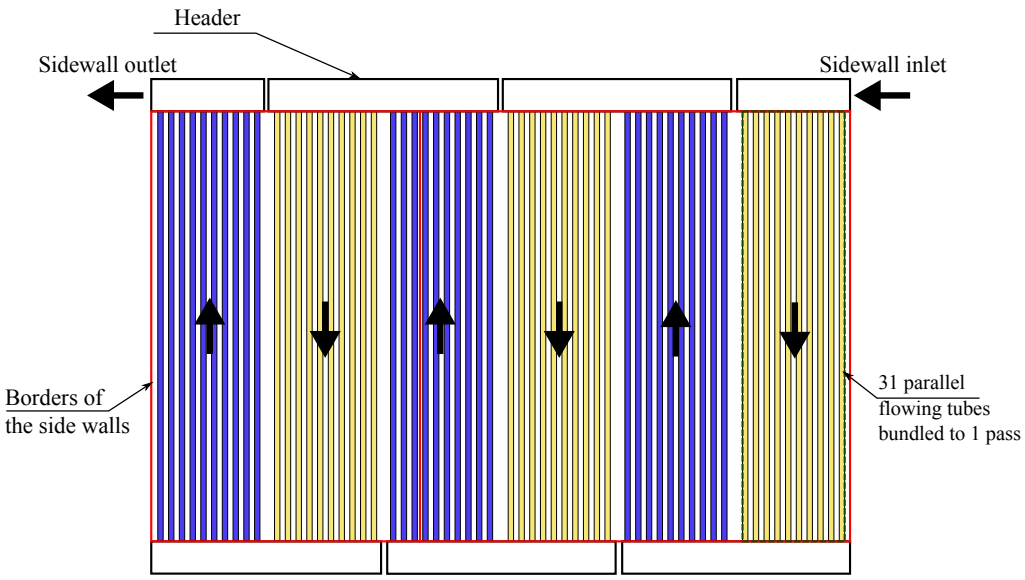

Figure 5.2: Scetch of tube layout in the projected sidewalls [3]

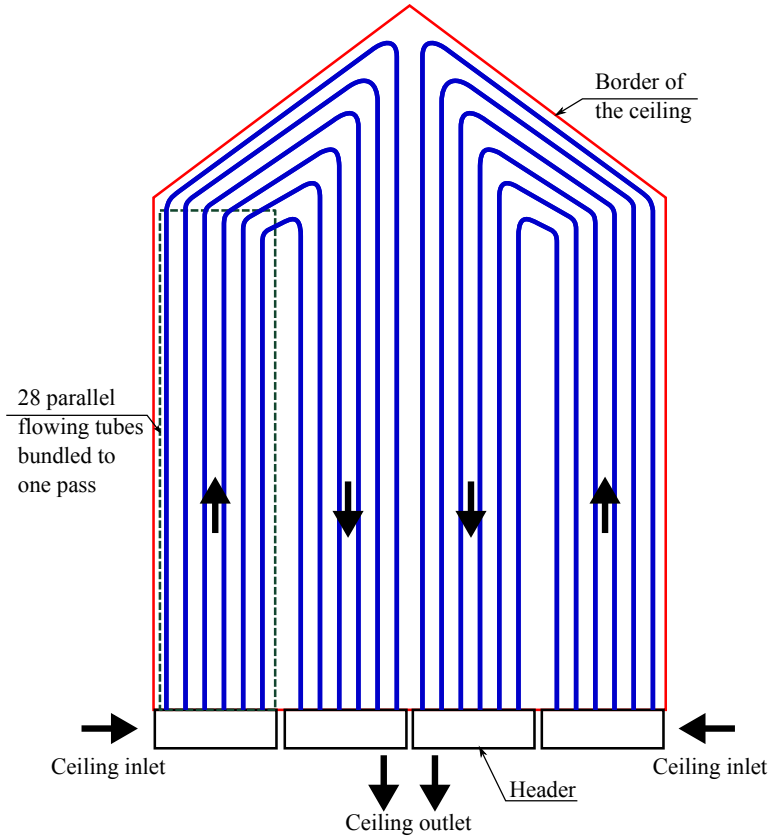

Figure 5.3: Scetch of tube layout in the ceiling [3]

5.1 Receiver- and other piping

The active parts of the receiver consist of the tube-walls, which are mounted on the east, southeast, west, southwest and ceiling walls. The inner diameter of each tube is 18.6 mm whereas the outer diameter is 25 mm. The tube pitch is given by 35 mm. These diameters are adopted form the preliminary work of [19] to increase the comparability. The thickness could also be decreased, since solar salt is used instead of water or steam. The reason for this is the lower pressure in case of salt. Nevertheless, the tube dimensions are kept the same. For the chosen dimensions of the tubes, the resulting number of the tubes of the particular structure are shown in table 5.1. The tubes are pooled together as passes to transport the required overall mass-flux with an acceptable mass-flux-density (1200 $\frac{kg}{m^2 s}$). They are arranged in vertical passes in the side walls (Figure 5.2), with headers at the top and the bottom of each pass and as parallel serpentines in the ceiling (Figure 5.3). The required nominal mass flux is calculated by the following equations (5.1 - 5.3). In these formulas $c_p(T)$ (5.1) is the heat capacity of the salt in dependence of the temperature. It is averaged by the temperature span of the inlet and outlet of the receiver and set into the first law of thermodynamics (5.2) to calculate the specific enthalpy difference between inlet and outlet of the receiver. The equation (5.3) gives us the required overall mass flow to heat up the salt to the required outlet temperature for the given nominal thermal capacity of 8.5 MW. This mass-flow is split up in two halves, so that each pass has to transport about 10 kg salt per second. The diameter of the feed pipes of the downcomer pipes is chosen with 10 cm to limit the flow velocity to less than 3 $\frac{m}{s}$.

$$c_{p_m} = \frac{\int_{T_i}^{T_a} c_p(T)}{T_a - T_i} = 1515.67 \ \frac{J}{kgK} \tag{5.1}$$

$$\Delta h = c_{p_m} * (T_a - T_i) = 416.8 \frac{kJ}{kg} \tag{5.2}$$

$$\dot{m} = \frac{\dot{Q}_{in}}{\Delta h} = 20.39302 \ \frac{kg}{s} \tag{5.3}$$

Table 5.1: Tube layout of the receiver

Structure	ceiling	west or east wall	southeast or southwest wall	parallel flowing tubes of side wall	parallel flowing tubes of the ceiling
Number of tubes	114	115	71	31	28
Surface area in m^2	41.783	37.935	23.421	10.226	10.446

5.2 Design of the pumps

The purpose of the cold salt pump is to deliver enough salt to the inlet tank to ensure that its level never falls below 1.3 m. Due to the fact that the receiver needs a nominal mass-flux of about 20 $\frac{kg}{s}$, the pump has to provide at least this flow rate to prevent the inlet tank from emptying and in further consequence from diminishing the functionality of the receiver. Therefore the salt has to overcome an elevation difference of at least 98.5 meters (elevation plus height of the inlet vessel). Due to the pressure losses in the piping and the inlet control valve and to have a safety buffer if a higher mass flow is needed, the nominal head of the pump is chosen with $H_n = 115m$ and the maximum head is chosen with $H_m = 150m$. The required nominal volume flow amounts to $\dot{V}_c = 42.342\ \frac{m^3}{h}$. To determine a characteristic curves field, the correlation (5.4) is used, which is also employed by APROS for the calculation of the actual head (documented by [19]). For that correlation the density of the fluid, the rotation speed and the volume flow are used to calculate the actual head of the pump. The value of the nominal rotation speed s_n is defined in APROS with 40 %, whereas the nominal density ρ_n corresponds to the density of the molten salt at 285 °C. The basic form of the curves is approximated by a parabola (5.5). The hot salt pump is designed accordingly with the values: $H_m = 15m$, $H_n = 11m$ and $s_n = 50\%$.

$$H(\dot{V}, s, \rho) = H(\dot{V}, s_n, \rho_n) \cdot \left(\frac{s}{s_{nom}}\right)^2 \cdot \left(\frac{\rho}{\rho_{nom}}\right) \tag{5.4}$$

$$H(\dot{V}, s_{nom}, \rho_{nom}) = H_m - \left(\frac{H_m - H_n}{\dot{V}_n^2}\right) \cdot \dot{V}^2 \tag{5.5}$$

5.3 Design of the salt tanks

The purpose of the inlet vessel is to provide one minute of uninterrupted salt flow to the receiver with the required pressure, even in the event of pump failure or plugged components [23]. In case of such an event, the mirrors have to defocus and the receiver

has to be drained.[1] On the other end of the receiver, the outlet vessel has to store the contents from the inlet vessel for a period of at least one minute, if the downcomer pipes or valves are blocked. During this incident, the mirror field has to defocus and the pump has to be stopped [23]. These requirements are fulfilled with vessels of 1 m diameter and 1.5 m in height, which can store a constant input or output flow of $20\frac{kg}{s}$ up to 110 seconds (depending of the density of the fluid inside). The Cold Salt Tank and the Hot Salt Tank have to store salt for at least 16-hour uninterrupted supply of the receiver and the steam generation system respectively to ensure a 24 hour per day operation of the Solar Power Tower [23]. This requirement is fulfilled when using cylindrical tanks with a diameter of 10 m and a height of 10 m.

5.4 Summary of all dimensions

The following table 5.2 summarizes the most important dimensions of the solar tower components.

[1] Unfortunately, draining was not possible to simulate with APROS. See also section 6.5

Table 5.2: Main dimensions

	number	length	wall thickness	inner diameter	outer diameter
downcomer pipe	1	105 m	10 mm	100 mm	120 mm
feed pipe	1	95 m	10 mm	100 mm	120 mm
receiver tubes side walls	372	4.2 m	3.2 mm	18.6 mm	25 mm
receiver tubes ceiling	56	9.5 m	3.2 mm	18.6 mm	25 mm
supply pipe	1	7 m	5 mm	100 mm	110 mm
	height	diameter	fixed pressure	elevation	calculation nodes
inlet tank	1.5 m	1 m	0.35 MPa	97 m	1
outlet tank	1.5 m	1 m	0.1013 MPa	106 m	1
hot salt tank	10 m	10 m	0.1013 MPa	0 m	1
cold salt tank	10 m	10 m	0.1013 MPa	0 m	1
	max. head	nom. head	nom. density	nom. flow	nominal rotation speed
cold salt pump	130 m	115 m	1908.74 $\frac{kg}{m^3}$	0.0113 $\frac{m^3}{s}$	40 %
hot salt pump	15 m	11 m	1733.84 $\frac{kg}{m^3}$	0.0113 $\frac{m^3}{s}$	50 %

5.5 Heat loss calculation

The heat losses of the receiver are calculated with a steady-state model at global level as shown in [15]. That means that changes of the parameters of the systems have to be assumed as quasi-static, which is a simplification of the real world conditions. The total energy balance of the receiver is given in equation (5.6), where the incident solar radiation $\dot{Q}_{in}$ is the sum of the total heat losses $\dot{Q}_{tot,loss}$ and the energy, which is absorbed by the salt $\dot{Q}_{abs}$.

$$\dot{Q}_{in} = \dot{Q}_{tot,loss} + \dot{Q}_{abs} \tag{5.6}$$

The total heat loss is composed of the convective loss of the aperture, the emissive and the reflective losses through the aperture, and the heat conduction through the wall. The absorbed energy $\dot{Q}_{abs}$ is the power input that is used for the APROS model.

5.5.1 Properties of air

The physical properties of air are needed to work out the Nusselt number for the heat loss calculation. These properties are found in tabular form[2] in [11] in dependence of the temperature. With this values of the density 5.7, the heat capacity 5.8, the dynamic viscosity 5.10 and the thermal conductivity 5.9 of air are approximated by the polynomials[3] given below.

$$\rho_{air}(T) = (1.26 - 4.03 * 10^{-3} \cdot T + 8.531 \cdot 10^{-6} \cdot T^2 - 7.763 \cdot 10^{-9} \cdot T^3) \frac{kg}{m^3} \tag{5.7}$$

$$c_{p\_air}(T) = (1.006 + 1.047 * 10^{-5} \cdot T + 4.836 \cdot 10^{-7} \cdot T^2 - 2.915 \cdot 10^{-10} \cdot T^3) \frac{kJ}{kg \cdot K} \tag{5.8}$$

$$\lambda_{air}(T) = (25.151 + 0.064 \cdot T) \cdot 10^{-3} \frac{W}{m \cdot K} \tag{5.9}$$

$$\eta_{air}(T) = (17.311 + 0.048 \cdot T - 1.924 \cdot 10^{-5} \cdot T^2) \cdot 10^{-6}\, Pa \cdot s \tag{5.10}$$

5.5.2 The emissive heat loss

Following the argumentation of [15], only the heat exchange between the the receiver surface and aperture was considerd. The heat transfer between different parts of the receiver was neglected to diminish the complexity of the calculation. ϵ_{avg} is the average emissivity of the cavity surface (chosen with $\epsilon_w = 0.95$ [9]) and of a black body ($\epsilon_w = 1$). The receiver surface area $A_{re,sur}$ divided by the aperture area A_{ap} gives the view-factor F_r and the Stefan-Boltzmann constant is given with $\sigma = 5.67 \cdot 10^{-8} \frac{W}{m^2 \cdot K^4}$.

$$\dot{Q}_{em} = \epsilon_{avg} \cdot \sigma \cdot \left(T_{re,sur}^4 - T_a^4\right) \cdot A_{ap} \tag{5.11}$$

$$\epsilon_{avg} = \frac{\epsilon_w}{\epsilon_w + (1 - \epsilon_w) \cdot F_r} \tag{5.12}$$

5.5.3 Reflective heat loss

The reflective heat loss through the aperture is calculated by the equation 5.13. According to [14] the reflectivity is assumed with $\rho = 1 - \epsilon_w$. The change of reflectivity with temperature is neglected.

$$\dot{Q}_{ref} = \dot{Q}_{in} \cdot F_r \cdot \rho \tag{5.13}$$

[2] Chapter D 2.2 "Tabelle 1" in [11]

[3] The values of temperatures T in °C have to be inserted without the dimension.

5.5.4 Convective heat loss - forced convection

Forced convective heat loss was modeled as forced convection from a flat plate with the geometry of the aperture of the receiver, which has the average receiver surface temperature. This reference temperature $T_{m,ins}$ is used to determine the properties of air ($c_{p,air}$, λ_{air}, η_{air} and ρ_{air}) and is given by equation (5.16). The characteristic length is the diameter of the aperture ($D_{ap} = 3m$) and the characteristic velocity to determine the Reynolds number is the windspeed that is picked out of the weather data of [3].

$$\dot{Q}_{con,fc} = h_{air,fc} \cdot (T_{re,sur} - T_a) \cdot A_{ap} \tag{5.14}$$

$$Nu_{con,fc} = 0.0287 \cdot Re_{air}^{0.8} \cdot Pr_{air}^{1/3} \tag{5.15}$$

$$T_{m,ins} = \frac{T_{re,sur} - T_a}{2} \tag{5.16}$$

5.5.5 Convective heat loss - natural convection

The natural convective heat loss is given by equation (5.17) and the required heat transfer coefficient is given by (5.18)

$$\dot{Q}_{con,nc} = h_{air,nc} \cdot (T_{re,sur} - T_a) \cdot A_{re,sur} \tag{5.17}$$

$$h_{air,nc} = 0.81 \cdot (T_{re,sur} - T_a)^{0.426} \tag{5.18}$$

5.5.6 Conductive heat loss

The conductive heat loss of the insulation layer has to be calculated iteratively by the formula (5.19) and is equal to the convective heat loss on the outer surface of the cavity. The conduction heat loss of the support structure is neglected. The insulation consists of 2 cm[4] mineral wool.

$$\dot{Q}_{cond} = \frac{(T_{re,sur} - T_a)}{\frac{\delta_{insuw}}{\lambda_{insuw}}} A_{re,sur} = (T_{insuw} - T_a) \cdot h_{air,outs} \cdot A_{re,sur} \tag{5.19}$$

The combined convective heat transfer on the outer shell of the cavity is calculated by adding the heat transfer coefficients of natural and forced convection.

$$h_{air,outs} = h_{air,outs,nc} + h_{air,outs,fc} \tag{5.20}$$

The following formulas show that the convective heat transfer coefficients are highly dependent on the temperature of the insulation wall. Therefore to calculate the heat

[4]This value was accidentally chosen too small, but a change would have made it necessary to repeat all simulations. For the reason of lack of time, the value was not changed. According to supervising professor Markus Haider a thickness of 20 cm would be more appropriate.

loss, one has to determine the temperature T_{insuw} first by iteration. The characteristic length is assumed as half the circumference of the receiver.

$$Nu_{fc,outs} = 0.0239 \cdot Re_{air,outs}^{0.805} \left(0.785 \cdot \frac{T_{insuw}}{T_a}\right)^{0.2} 1.167 \cdot Pr_{air,outs}^{0.45} \tag{5.21}$$

$$h_{air,outs,nc} = 1.24 \cdot (T_{insuw} - T_a)^{1/3} \tag{5.22}$$

5.6 Discussion of the heat loss calculation

Due to the fact that the chosen heat loss model has a significant impact on most of the simulation results, the determining parameters of this model are discussed below. To assess how much the heat loss calculation influences the temperature curves, some typical values are viewed and compared to the solar input (Table 5.3). Furthermore, the model is compared to the results of preliminary works.

Table 5.3: Representative results of the heat loss calculation - The simulation was run in normal operation mode after a hotstart with constant solar input ($\dot{Q}_{in}$=7.815 MW), ambient temperature (36.6 °C) and wind speed (3 $\frac{m}{s}$)

	Conduction loss	Emissive losses	Forced convection loss	Natural convection loss	Reflective loss	Overall losses
Absolute values in kW	45.07	110.23	19.25	332.14	132.21	638.91
Relative values	7.05 %	17.25 %	3.01 %	51.99 %	20.69 %	100 %
relative values compared to $\dot{Q}_{in}$	0.58 %	1.41 %	0.25 %	4.25 %	1.69 %	8.18 %

In the table above one can see that the heat loss reduces the absorbed energy by about 8 % of the arriving solar input. As a consequence the receiver efficiency amounts to about 92 % in nominal operation. Therefore a visible effect on the temperature curves of the hot-start (section 7.1) and the whole-day simulation (section 7.5) can be assumed. Considering that after shutdown (section 7.2-section 7.4) the heat loss is the only thermodynamic effect affecting the system at its boundaries, its impact is expected to be even higher than in other operation modes. For that reason it is important to know how accurate the heat loss model is and what the determining parameters are. Another interesting aspect found in table 5.3 is that the natural convection on the inside of the receiver is higher than the forced convection through the aperture. Despite the fact that

the forced convection should dominate the natural convection on the outside of the receiver [5], the situation is the opposite on the inside of the current pentagonal receiver. This has two reasons:

1. The cavity design reduces the velocity of the air-stream (Figure 5.4)and therefore the forced convection heat losses as shown by [8].

2. The results are highly dependent on the area that is used in the formula of the heat loss (5.14). In this master's thesis the forced convection of the receiver is modeled as forced convection of a hot plate with the dimensions of the aperture (following the argumentation of [15]), which is why its area is chosen for the heat loss calculation. If the whole surface of the receiver wall was used, the resulting losses would be much higher.

Influence of the receiver geometry In the preliminary work of [8], the influence of the wind around the receiver on the forced convection heat losses is examined. In particular the velocity field of the air around and in a cubic cavity receiver with no aperture lips was investigated. The results show that the cavity configuration decreases the velocity on the active receiver walls (Figure 5.4) and the heat transfer coefficient significantly[6]. In other words, the forced convective heat loss is substantially lower compared to other receiver designs.

Influence of the chosen parameters To show the impact of the chosen reference area, the selection for each type of heat loss is discussed below.

- The tube-walls constitute the radiating part of the receiver. Therefore, the surface of the active receiver walls is used for the calculation of the emissive heat losses. This surface has to be multiplied with the view factor and leaves the aperture area after reducing the fraction.
  $(A_{ap} = F_r \cdot A_{re,sur} = \frac{A_{ap}}{\cancel{A_{re,sur}}} \cdot \cancel{A_{re,sur}})$

- The reflective heat losses are calculated with the view factor, which is explicitly defined as the ratio of the aperture area to the receiver surface area.

- The conductive heat losses are calculated with the surface area of the active receiver walls (according to [15]).

- The surface area of the active receiver walls is used for the natural convection loss of the cavity (according to [20] or [15]). This seems to be logical because natural convection is driven by the temperature difference of the receiver surface to the surrounding air.

[5] Annotation of supervising professor Markus Haider

[6] The heat transfer coefficient of the cavity receiver is about 25-50% of the heat transfer coefficient of the conventional external receiver

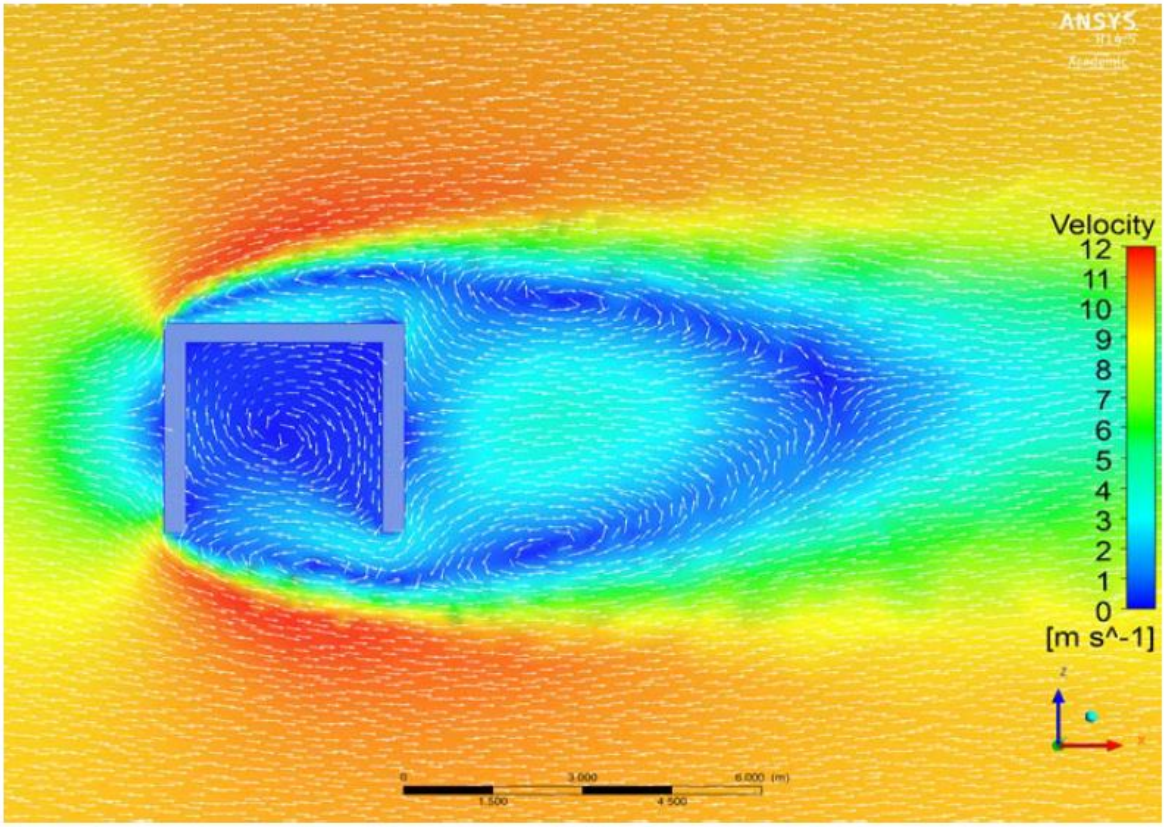

Figure 5.4: Velocity distribution around and in the cavity receiver [8]

- It is obviously very difficult to receive reliable results of the analytic calculation of the forced convection, because of imprecise assumptions that have to be made. The velocities of the air streams inside the cavity are highly complex and hard to predict for the current geometry of the receiver (See also [20]). CFD calculation could be used improve the model but this was not in the scope of this work. For that reason the calculation of this thesis follows a simple model of [15] which simulates the forced convection losses as losses of a hot plate with the size of the aperture. This is expected because the wind speed is highest near the aperture, as illustrated in 5.4. The current model states that the forced convection inside the receiver is not as important as the natural convection. Further parameters of the forced convective heat loss calculation, which influence the results are the chosen reference remperature (Equation 5.16) and the characteristic length (Diameter of the Aperture).

Conclusion There are too many uncertain assumptions that have to be made for the heat loss model to guarantee 100 % accuracy of the results. Nevertheless the model helps to predict the fundamental behavior of a system. Experiments have to be made to find out how close the results of the model are to the reality.

5.7 Pressure loss of the receiver

The following pressure loss calculation is based on [22]. This section deals with the pressure losses due to friction and form losses, that occur in the receiver tubes between the inlet tank and the outlet tank. In general, pressure losses are calculated by an equation in the form of (5.23). The pressure losses due to friction in the header are neglected [7].

$$\Delta p = \frac{\zeta \cdot \rho \cdot w^2}{2} \tag{5.23}$$

The following properties are used in the formula above: ζ is the resistance factor, ρ is the density of the fluid in the tube and w is the average velocity.

5.7.1 Tube friction

For a given diameter ($d_i = 18.6\ mm$) and an absolute (hydraulic) roughness of $K = 0.006\ mm$ the friction factor ξ_{rough} is calculated by:

$$\xi_{rough} = \left(1.14 + 2.2 \cdot lg\left(\frac{d_i}{K}\right)\right)^{-2} \tag{5.24}$$

With that, the resistance factor is given by:

$$\zeta_{rough} = \xi_{rough} \cdot \frac{L}{d_i} \tag{5.25}$$

5.7.2 Deflection, inlet and outlet losses

According to [22] the resistance factor can be assumed as $\zeta_{inlet} = 0.5$ for the inlet flow from the header to one tube, if the velocity of the fluid in the header is neglected compared to the velocity in the tubes. Furthermore the value of ζ_{outlet} can be chosen with 1 for the outlet flow from the tube into the header. Last but not least $\zeta_{deflection}$ is calculated by the following equation for the deflection between one vertical panel and another ($\delta = 180°$) in serpentine flow arrangement:

$$\zeta_{deflection} = \xi_{rough} \cdot f_u \cdot \sqrt{\frac{\delta}{90°}} \tag{5.26}$$

Where f_u is a factor dependent to the fraction $\frac{R}{d_i}$ with the radius R of the U shaped piece that connects two tubes. This factor can be picked out of tables as given in [22].In this work a value of $f_u = 9.05$ is used.

[7] As a simplification, the velocity in the headers is assumed negligible in that structure.

5.7.3 Overall losses

The previous formulas result in the pressure losses shown in table 5.4, which are valid for a nominal mass flow of 20 $\frac{kg}{s}$ for the receiver and an average density of $\rho = 1821.29\ \frac{kg}{m^3}$ in the temperature range of 285-560 °C. These properties correspond to an average flow velocity of $w = 0.665 \frac{m}{s}$ in the receiver tubes.

Table 5.4: Average resistance and pressure losses of one tube in the given structure

side walls/vertical panels			ceiling/ serpentine flow	
ζ_{rough}	ζ_{inlet}	ζ_{outlet}	ζ_{rough}	$\zeta_{deflection}$
5.151	0.5	1	11.651	0.292
Δp_{rough}	Δp_{inlet}	Δp_{outlet}	Δp_{rough}	$\Delta p_{deflection}$
0.02072 bar	0.00201 bar	0.00402 bar	0.04687 bar	0.00117 bar

Provided that the mass flow of the receiver is split equally between two flow paths, and the previous assumptions are still valid, the overall receiver losses are calculated by (5.29). The pressure loss due to inlet flow, outlet flow and friction of one tube in the side walls are summed up and multiplied by 6 (caused by the 6 vertical passes that the salt has to flow through). After ingress in the ceiling part of the receiver the salt has to travel an average distance of 9.5 m with one deflection of 180°. Therefore inlet, outlet, friction and deflection losses from table 5.4 are added to receive the whole pressure loss in the ceiling. Accordingly, the pressure losses of the ceiling and of the sidewalls are added together.

$$\Delta p_{sidewalls} = 6 \cdot (\Delta p_{rough,sw} + \Delta p_{inlet} + \Delta p_{outlet}) \tag{5.27}$$

$$\Delta p_{ceiling} = \Delta p_{rough,ce} + \Delta p_{deflection} + \Delta p_{inlet} + \Delta p_{outlet} \tag{5.28}$$

$$\Delta p = \Delta p_{ceiling} + \Delta p_{sidewalls} = 0.205 bar \tag{5.29}$$

If the pressure loss of the supply pipe ($\Delta p_{supply} = 0.0427$) and the pressure loss of the control valve ($\Delta p_{valve} = 1\ bar$) at nominal point are also considered, the overall pressure loss between the inlet and the outlet tank is $\Delta p_{all} = \Delta p + \Delta p_{valve} + \Delta p_{supply} = 1.257\ bar$.

6 Apros model

As mentioned before, the dynamic simulation modeling software "APROS" is used to examine the dynamic behavior of the solar salt receiver. In this chapter the modeling process is described and the chosen boundary conditions are listed to guarantee the repeatability of the results.

6.1 Material properties

To ensure the highest possible quality of the results, the properties of the working fluid and the receiver tube material have to be adapted. Therefore the formulas, described in the following subsections are taken as input for the simulation software.

6.1.1 Solar Salt

One of the key tasks in dealing with the APROS software is to implement a reliable model of solar salt as heat transfer fluid and to deal with the problems originating from that. The simulation has to be adapted by using the available fluid module "OIL" and give it the thermodynamic properties of the solar salt in form of the formulas below[1]. The heat capacity (6.1), the density (6.2), the dynamic viscosity (6.3) and the conductivity are given by polynomials recommended by [23].It is not possible to simulate freezing at low temperatures or decomposition at high temperatures of the salt because this features are not realized for the "OIL" module. Therefore one has to be careful to use the formulas and in further consequence the results of the simulation just for the range of validity (260°C- 620°C).

$$\text{Heat Capacity} \quad c_p(T) = (1443 + 0.172 * T)\ \frac{J}{kgK} \tag{6.1}$$

$$\text{Density} \quad \rho_{salt}(T) = (2090 + 0.636 * T)\ \frac{kg}{m^3} \tag{6.2}$$

$$\eta_{salt}(T) = (22.714 - 0.120 \cdot T + 2.281 \cdot 10^{-4} \cdot T^2 - 1.474 \cdot 10^{-7} \cdot T^3)\ Pa\,s \tag{6.3}$$

[1] The values of temperatures T in °C have to be inserted without the dimension.

$$\lambda_{salt}(T) = (0.433 + 1.9 \cdot 10^{-4} \cdot T) \cdot \frac{W}{m \cdot K} \tag{6.4}$$

6.1.2 High nickel alloy steel

High nickel alloy stainless steel is chosen as the material of the tube-walls, specifically ASTM A312, Type 321/347 as commenced by [23]. This designation of the "American Society of Testing and Material" (ASTM) corresponds to the DIN steel X6CrNiTi19-10 [16]. The thermodynamic properties of the steel are taken from the tables of [11] and [5] interpolated by a regress function in Mathcad[2]. The following formulas describe the 0.2 % yield strength (6.5) and the conduction (6.6) of the steel dependent on the temperature in °C. These formulas where used to define a new APROS solid material[3].

$$\sigma_{0.2\%}(T) = \big(0.465 - 3.779 \cdot 10^{-4}T - 6.362 \cdot 10^{-7} \cdot T^2 + 9.317 \cdot 10^{-10} \cdot T^3 \ldots \\ -5.369 \cdot 10^{-13} \cdot T^4\big)\ MPa \tag{6.5}$$

$$\lambda_{steel}(T) = \big(0.025 - 1.285 \cdot 10^{-5}T - 1.492 \cdot 10^{-7} \cdot T^2 + 2.535 \cdot 10^{-10} \cdot T^3 \ldots \\ -1.282 \cdot 10^{-13} \cdot T^4\big)\ \frac{W}{m \cdot K} \tag{6.6}$$

6.2 Input data

The boundaries of the modeled system are the outer surfaces of the tubes, tanks, pumps and valves. Therefore the impact of the focused sunlight of the mirror field has to be simulated. This was done by providing the solar input in form of a heat-flux-density in each node of the receiver tubes. On the one hand some typical values of constant solar irradiation for each active receiver wall, ambient temperature and wind speed are given in an input file and imported by the software (Table 6.1), on the other hand, real weather data is imported by a file with values that are varying with time (Figure 6.1). The measurements of the weather data start at 5:40 in the morning of May 19th, 2012.

[2]Mathcad is an engineering math software by PTC

[3]The values of temperatures T in °C have to be inserted without the dimension.

Table 6.1: Input data

Solar input for each wall						
east	southeast	southwest	west	ceiling	ambient temperature	wind speed
1.81049 MW	1.06884 MW	1.04033 MW	1.72538 MW	2.17032 MW	36.6 °C	3 $\frac{m}{s}$
47.73 $\frac{kW}{m^2}$	45.64 $\frac{kW}{m^2}$	44.42$\frac{kW}{m^2}$	45.48 $\frac{kW}{m^2}$	103.89 $\frac{kW}{m^2}$	36.6 °C	3 $\frac{m}{s}$

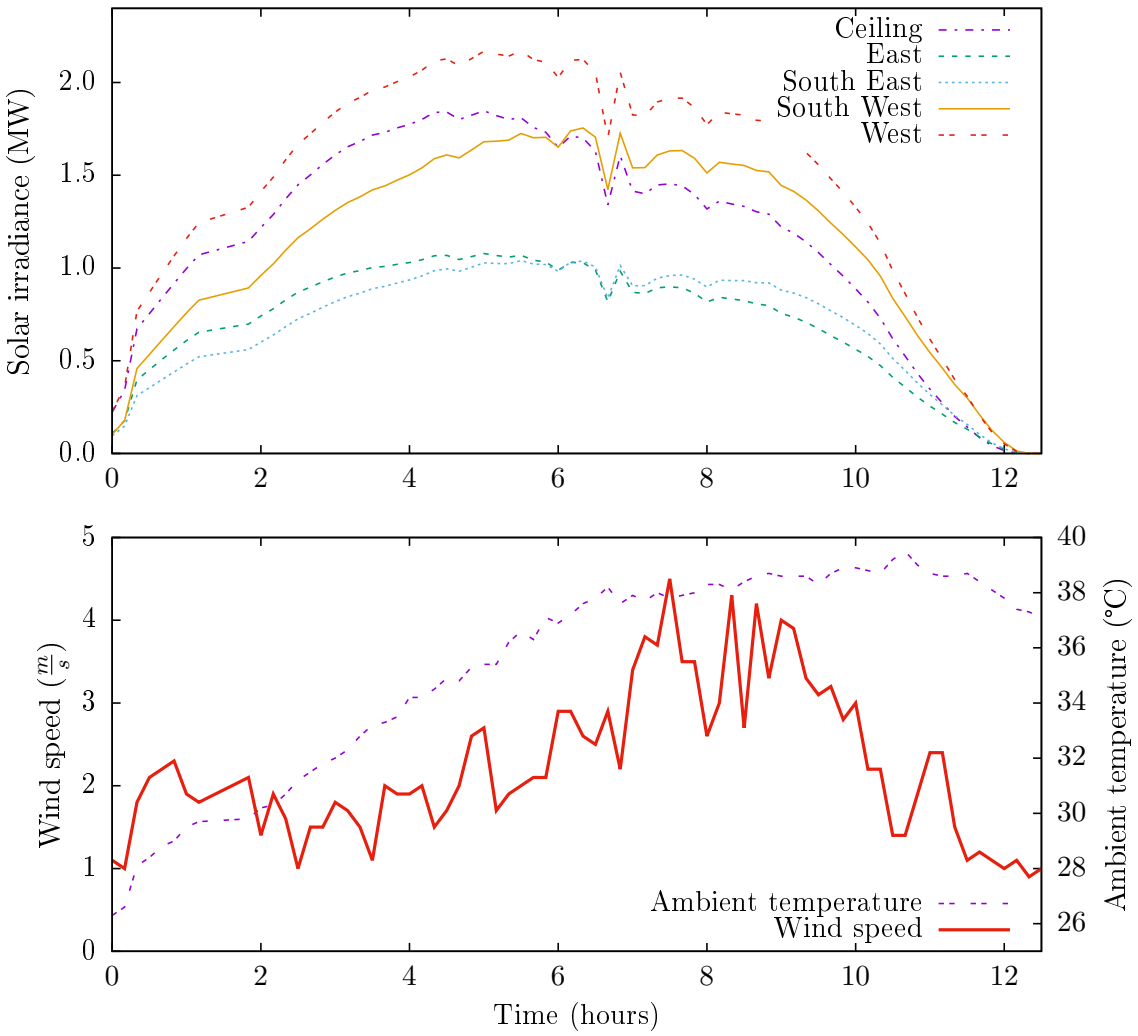

Figure 6.1: Illustration of the input data of [3]

6.3 Process modeling

In this section the whole APROS simulation process model is described. The main components of the model are the tank, control valve, pipe with heat structure, pump and point modules. These modules where connected as shown in the process diagrams (Figure A.1 and Figure A.2), to build up a model as realistic as possible. The modules were given descriptive names in the diagrams to help the observer understanding how the system was modeled and how it is meant to work. Nevertheless a short introduction in the behavior of the model in given below.

6.3.1 Basic process

The basic cycle process (Figure A.1) shows how the salt is used as a heat transfer fluid to produce electricity. It is pumped by the cold salt pump from the cold salt tank into the inlet tank. The "inlet control valve **1**" prevents the back-flow in normal operation mode. In contrast, the "inlet control valve" stops the back-flow from the inlet tank in stand by mode and is just needed to prohibit unrealistic flow from the inlet tank (see also section 6.5). The inlet tank provides the pressure to pump the salt to the outlet tank through the receiver ("Flow path 1 "- Figure A.2), where the salt absorbs the solar energy. From there the salt is headed back in the cold salt tank as long as the salt temperature remains below 500°C and otherwise in the hot salt tank. A required amount of salt is pumped trough the steam generation system back to the cold salt tank. The steam generation system is represented by the steam generation pipe. This is basically a "pipe with heat structure" module. The desired power, which an assumed steam generation heat exchanger draws, can be controlled with the attribute "heating power". This property has to have a negative value to satisfy the release of energy of the salt system.

Receiver: The receiver is consisting of a row of "pipe with heat structure" modules. Each pipe module represents one pass, consisting of a bundle of single tubes [4]. The modules were discretized with 4 nodes and 5 branches in the side walls and by 8 nodes and 9 branches in the ceiling. The solar input absorbed by the module is controlled by the attribute HSN_HEAT_FLUX of the nodes. Because of the unsatisfactory options to model the headers with the tank or the pipe modules, the headers are modeled with point modules. Therefore the influence of the headers is only considered in the flow resistance which is added to the resistance of the pipe modules. The salt flow is split up into two mirrored flow paths namely east and west. These two receiver halves are modeled exactly the same way.

Tanks: Four tank modules are used in the APROS model for the solar power tower. To model the properties of a tank structure, one should first define a volume with certain dimensions which is then filled with salt to retrieve values for the amount of salt and

[4] See also section 5.1

air in the tank and the level of the liquid. Unfortunately this indispensable feature was not easily available and caused a lot of other problems [5]. To gain this desired behavior of the tanks, it seems to be absolutely essential to use the values given in Table 6.2 for the specific attributes listed there. The remaining attributes are more or less arbitrary within the frame given by the APROS documentation [1]. Finally it was possible to simulate partially filled tanks and acceptable results were achieved for the simulated operation states.

Table 6.2: Essential attributes for tanks

Attribute	is pressure solved	number of calculation nodes	is fixed pressure solved	name of fluid
Value	0	1	1	OIL

Pumps: The pumps are used to increase the pressure in the fluid and to generate a flow. This module needs the values for the nominal head and nominal mass-flow as well as the maximum head which determines the volumetric flow-head curve. The pump speed is controlled by means of the attribute PU11_SPEED_SET_POINT. Table 6.3 shows which values are chosen for the hot salt pump or the cold salt pump. The other attributes kept their default values.

Table 6.3: Non-default attributes of the pumps

	maximum head	nominal head	nominal rotation speed	nominal flow	speed set point
Cold salt pump	130 m	115 m	40%	0.0113 $\frac{m^3}{s}$	5 s
Hot salt pump	15 m	11 m	50 %	0.0113 $\frac{m^3}{s}$	5 s

Valves: Valves are used to regulate the liquid flow through the valve, by calculating the flow area of the valve as a function of the valve position. It is opened or closed by means of setting the attribute VA11_POSITION between 0 and 1. Most attributes were left as default. The material of the valve is changed according to subsection 6.1.2, the driving time (closing/opening time) of the valve was changed to 5 seconds and the nominal density was inserted with 1908.74 $\frac{kg}{m^3}$.

Points: Points are used to connect different kinds of process components together [1]. Points and tanks are the only modules used, where the elevation from reference level is

[5] see also the restrictions section 6.5

an attribute that has to be given. Thus, points are mainly used to connect two tubes and define the elevation of the endings of the tubes.

6.3.2 Automation & control system

The purpose of the automation and control system is on the one hand to regulate the flow in different parts of the systems and on the other hand to steer the mirror field and the aperture. This duty was fulfilled by controlling the valve positions, the pump speed, the level of focus of the mirror field and the aperture position. Also logic circuits are used to model various operation transitions like closing the aperture. Figure A.8 Figure A.10

Flow control The receiver itself has to provide an as constant as possible outlet temperature of 560°C. Therefore the mass flow in each receiver path has to be regulated according to the available solar input. The temperature at the end of each path is measured and taken as control variable for the PID[6] controllers which regulate the valve position of the control valve 1 and 2 respectively. Also the flow between the hot and the cold salt tank is regulated by a control valve, which valve position is determined with its own PI[7] controller. The used attributes for these controllers were given in Table 6.4 below.

Table 6.4: PID controller

	Direct operation?	Gain	Integral time	Derivative time	Local setpoint used?	Output minimum
Control valve 1 & 2	false	3	800	20	false	0.05
"Steam generation" valve	true	10	500	-	false	0.05

Inlet tank control The purpose of the inlet tank is provide backup salt with a fix sufficient pressure to overcome the flow resistance and the height of the receiver. Its level is controlled by the "inlet valve **1**" and the cold salt pump, which in turn are controlled by a control circuits shown in Figure A.6.

Outlet tank control The "outlet control valve" and the "back to cold tank valve" are controlled by the logical circuits and the controller shown in Figure A.7 ,in a way that the flow is lead back to the cold salt tank, if the outlet salt temperature is below 500°C and to the hot salt tank if it is above.

[6]Proportional-integral-derivative
[7]Proportional-integral

Heat loss control Because of poor options and insufficient description of the functional principle in the APROS documentation of simulating the heat transfer between the "pipe with heat structure" and an environment, the heat loss was calculated separately and implemented as the control system shown in Figure A.4. These circuits represent the formulas given in section 5.1.

Solar mirror field In the automation diagram Figure A.5 one can see how the conversion of the solar input in heat-flux-densities for the receiver nodes is implemented. For that, the heat losses are subtracted from the input data in form of the absolute solar irradiation power for each active receiver wall and divided by the area[8] of the surface of the receiver tubes. Also a focus/defocus sequence is modeled, where one can adjust how fast the mirror field is focused on the receiver in case of switching the state from stand by to normal operation and vice versa.

States The automation diagram A.9 shows that the states can be changed manually during the simulations by pushing buttons, but also can be changed automatically. The state switches from stand by to normal operation if the overall input exceeds 1.5 MW[9] and jumps back if the input falls below that value. This automatic switch is used for the whole-day simulation (section 7.5) only.

6.4 Piping heat losses

The heat losses were implemented in the APROS model in a way, that they are calculated in dependence of the average surface temperature of the receiver tubes T_{rp}, the ambient temperature T_{amb} and the wind speed w_s. They are subtracted from the solar input, and the result is used as the boundary condition at each node of the receiver tubes. The heat losses were weighted with the representative temperatures[10] of each receiver part. The basic principles of the heat loss calculation were given in section 5.5, but to keep the model as simple as possible the given equation system was simplified with "Mathcad". The Nusselt numbers and the heat-transfer coefficients were approximated (with high accuracy) by polynomials ((6.7),(6.8)) in dependence of T_{rp}, T_{amb}, w_s. The resulting expressions are given below.
The heat transfer coefficient for the forced convection heat loss through the aperture is

[8] See also 5.1

[9] This value is conforming to about 18% of the nominal duty of the receiver.

[10] The temperatures were taken from the node which approximately divides the flow path of the considered receiver wall in two halves. Therefore it corresponds roughly to the arithmetic average of the receiver wall. The exact average was not generated because it would overload the capacities of the computer and would have made working on the model unacceptably slow.

calculated by:

$$h_{fc}(T) = \big(9.593021 - 0.021365 \cdot T + 4.471476 \cdot 10^{-5} \cdot T^2 \ldots \\ -4.025 \cdot 10^{-8} \cdot T^3\big) \left(\frac{w_s}{w_{s0}}\right)^{0.8} \frac{W}{m^2 \cdot K} \tag{6.7}$$

with the average temperature $T = \frac{T_{rp}+T_{amb}}{2}$ in °C and the reference wind speed $w_{s0} = 3\frac{m}{s}$ The heat transfer coefficient for heat loss through outer shell is approximated by:

$$h_{cond}(T) = \big(11.80453 - 3.448588 \cdot 10^{-3} \cdot T - 3.318644 \cdot 10^{-6} \cdot T^2 \ldots \\ -3.777521 \cdot 10^{-9} \cdot T^3\big) \left(\frac{w_s}{wa_{s0}}\right)^{0.805} \frac{W}{m^2 \cdot K} \tag{6.8}$$

with the average temperature $T = \frac{T_{rp}+T_{amb}}{2}$ in °C and the reference wind speed $wa_{s0} = 5\frac{m}{s}$

6.5 Restrictions

Unfortunately it turned out that APROS was not able to simulate "Solar Salt" directly. Thus, it has to be approximated by giving the available fluid module "OIL" the physical properties of the solar salt[11]. But because of the specialization of APROS to water steam systems many features were not available for the modeling with the "OIL" fluid respectively solar salt. In the following a list of problems and restrictions that occurred is given without any claim of comprehensiveness:

- The usage of the fluid "OIL" is fixed to the 3 equation model of APROS fluids. Therefore it is not possible to simulate two phase fluids in the system. This leads to the following issues:
  - It was not possible to simulate draining of the tubes. For the draining process it has to be possible to air the system, which would lead to a two-phase fluid mixture of air and solar salt in some parts of the system, but that contradicts the definition of the 3-equation fluid model [12].
  - The draining of the tank did not work as described in the documentation. One has to find out the one specific configuration of attributes to make the model work right. For example it is not possible to discretize the tank with more than one node, for unknown reason.
  - In some parts of the system, in some operation states unrealistic pressures appeared.

[11] See also subsection 6.1.1
[12] See also subsection 4.2.1

- If the tanks were emptied in some operation modes, the flow out of the tank did not stop, even if there was no more salt in the tank. That means that if no extra valve was installed that stops the flow, the tank would work as a source.
- Exported complex models could not be imported on other computers and sometimes could even not be re-imported on the computer they were made.
- The calculation speed of the computer was limited. Complex models and complex diagrams lead to a long reaction time of the program. Therefore the model has to be held as simple as possible. For example fewer discretization nodes as wished could be used for the receiver tubes because they needed a lot of other modules to connect them to the model. This made the handling of the process diagram worse because it got stuck every time a change was applied.
- To model the header of the receiver panels the tank modules would have been best choice. Unfortunately, as mentioned before, the tank modules did not work the way they were expected to. One of the restrictions of the tank was the use of a fixed fluid pressure to simulate a variable fluid level. But these fixed pressures would lead to a unrealistic conditions of the receiver headers. Therefore the headers were not modeled at all. The effect on the storage of heat in these structures has been neglected. The pressure loss that would have been caused by the headers is calculated and assigned to the losses of the tube.
- The documentation for the built-in feature to simulate the heat loss of a tube was very poor. Therefore it was not possible to define the heat loss process exactly the way it was hoped for with that option and the heat losses were calculated separately as described in section 6.4.

To respond to these problems the simulation is limited to operation states were most of these problems do not emerge. For that reason, it was not possible to simulate draining. In some cases it was also possible to find another, maybe not very sophisticated way to avoid the restrictions, like the implementation of the heat loss model. Although APROS does not seem to be an excellent tool simulate a molten salt solar power tower, the results that are received (in chapter 7) are convincing.

7 Results

To receive informative statements about the dynamic behavior of the receiver or the whole salt cycle, three different operation transitions were examined. A "hot-start", several "shutdowns" and a "whole day simulation" were performed. Unfortunately it was not possible to simulate the draining of the system and therefore it was not possible to simulate a "long term hold" or an "overnight-hold" state, as described in detail in the restrictions section 6.5. For the simulation of the "Hot-start" and the "Shutdown" operation modes an input date file was produced with constantly high irradiation, ambient temperature and wind speed values, whereas the "whole-day" simulation was performed with an input file, created out of real weather data (see also 6.2). Besides the interest in the general behavior of the receiver, it is also important to check if none of the physical value exceeds the limits of the material. Theoretically, the salt could be used in a temperature range of 238°C, where it crystallizes, to 621°C where is degrades [23]. Because of the fact that the nominal usage scope of the salt is between 285°C and 560°C, it is dangerous to get in a area where degradation or cristalization could happen.

7.1 Hotstart

The operation mode "hotstart" simulates a situation of a suddenly high solar input, which could appear for instance after a severe cloud transition on an otherwise sunny summer day and is a tough test for the control system. The related curve of the solar input is illustrated by Figure 7.1. One can check if the controller reacts fast enough to prevent unacceptably high temperatures in the system, in which case the fluid or the tubes could be damaged. The following procedure was executed to simulate the "hotstart" operation transition: At first the receiver was spilled with Salt of about 285°C from the cold salt tank until the receiver tubes had an approximately constant temperature. The salt was lead to back to the cold salt tank after the outlet tank with a bypass to prevent hot salt tank from cooling. After that preparation the mirrors were focused on the receiver and the controller regulated the outlet salt temperature to a nominal value of 560°C and the "downcomer" pipe lead the hot salt to the hot salt tank. The resulting tube temperatures 7.2, salt temperatures 7.4, heat losses 7.3 pressures 7.5 in the receiver and mass-flows 7.6 for each pass are illustrated by the following diagrams.

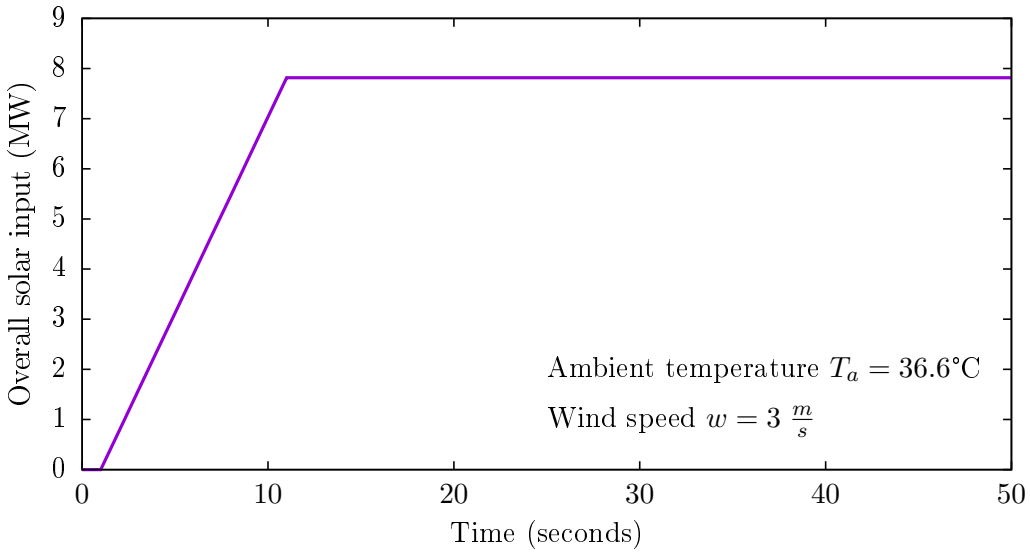

Figure 7.1: Solar input - hotstart

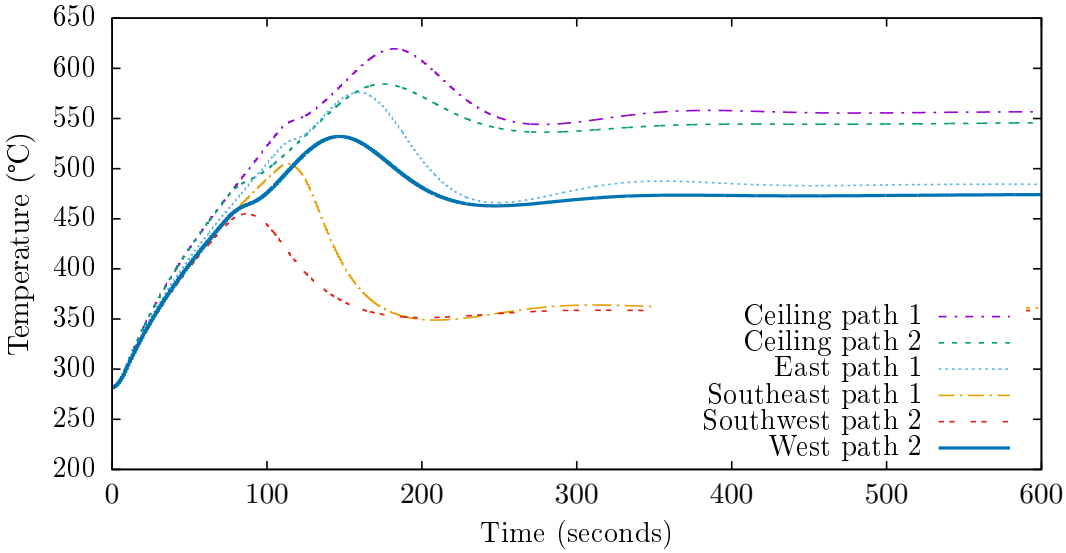

Figure 7.2: Temperatures on the surface of the receiver tubes - hotstart

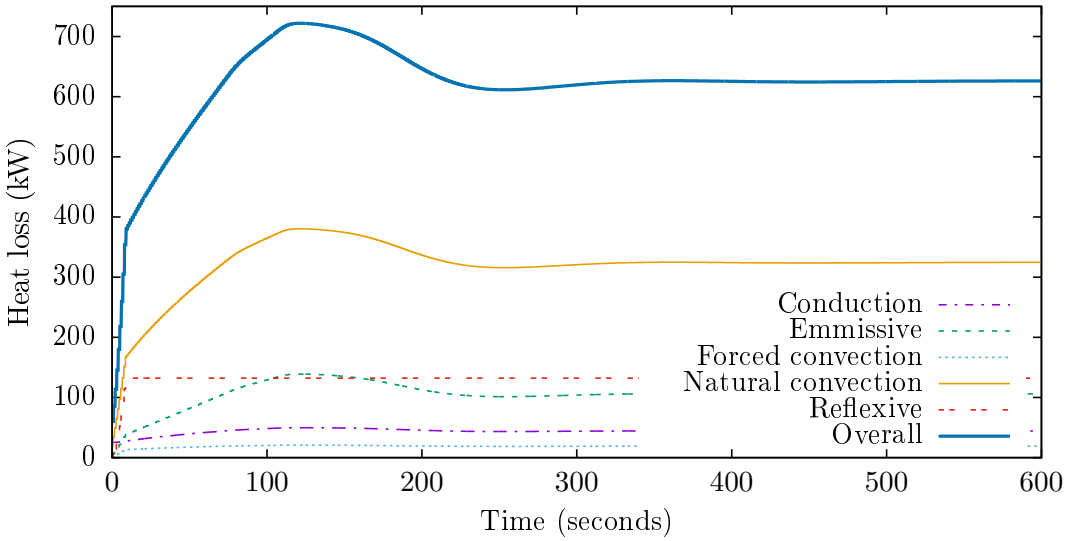

Figure 7.3: Receiver heat losses - hotstart

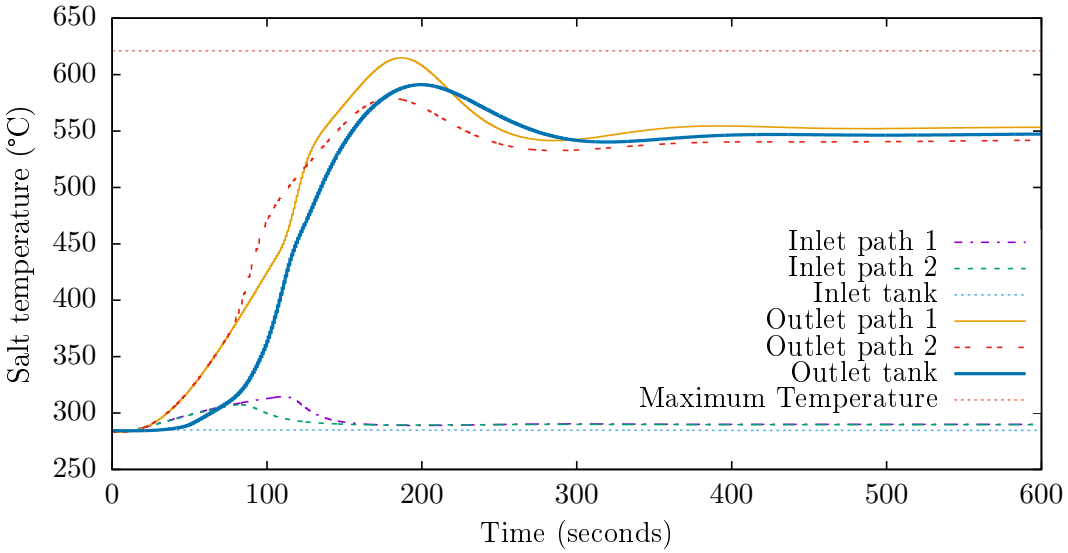

Figure 7.4: Salt temperatures - hotstart

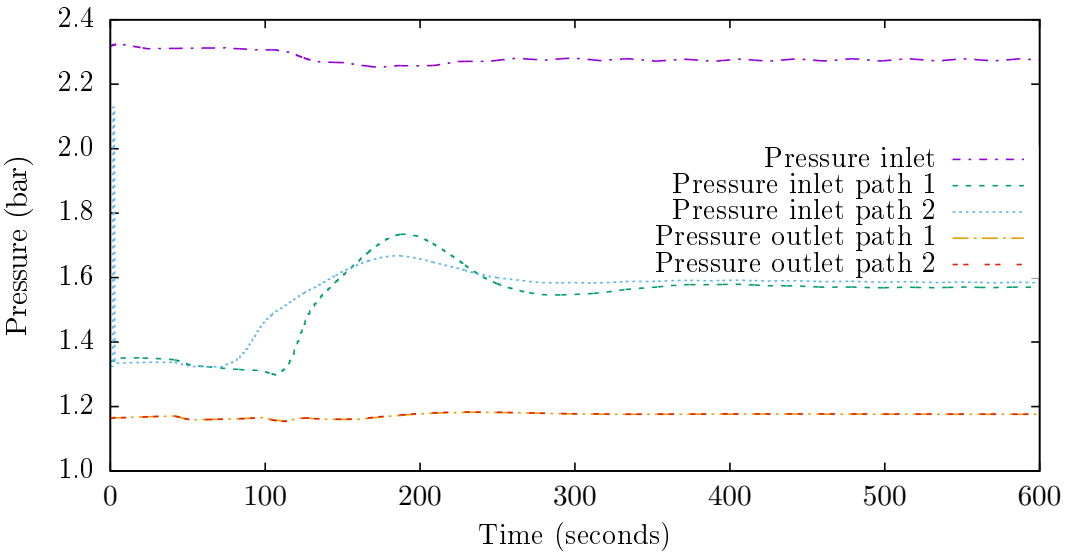

Figure 7.5: Pressures - hotstart

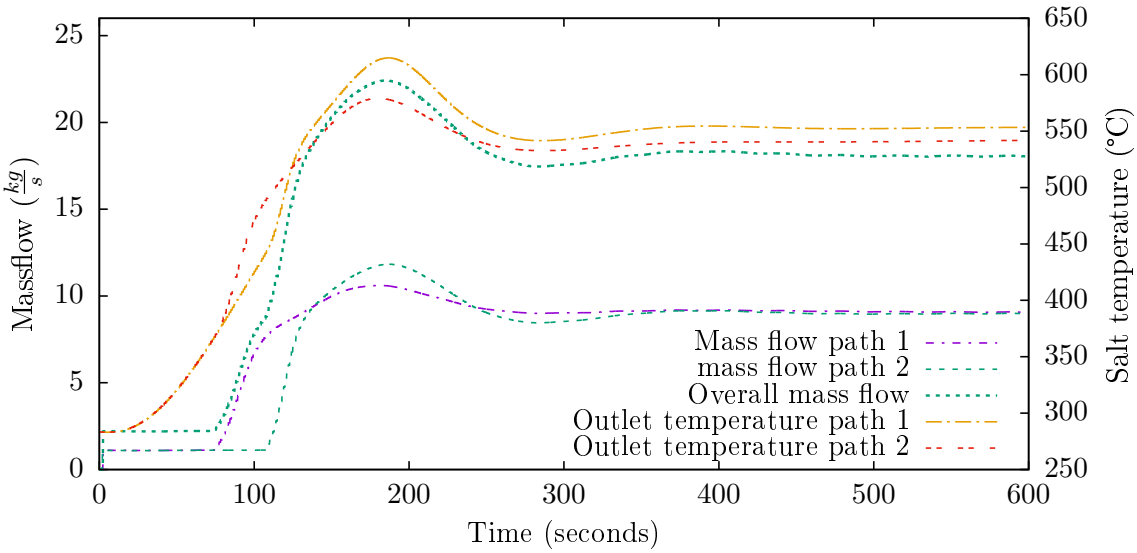

Figure 7.6: The mass flow on the first ordinate is compared to outlet salt-temperatures on the second ordinate - hotstart

7.2 Shutdown - AP10 V5 M10

The shutdown of the receiver is a very important, and sometimes critical situation during the operation of a solar thermal power plant, which happens at least one time a day. Besides the controlled shutdown at the end of the day, there are also unexpected or sudden situations where it is necessary to switch to the "stand by" mode very quickly, like cloud transitions or a defective component of the system. In the current "shutdown to stand by" mode the command is given by the user of the simulation program after a period of normal operation with constant weather data input. After pushing the "shutdown" button[1] the control valves are closing within 5 seconds (V5), the mirror is defocusing within 10 seconds (M10) and the aperture is closed within 10 seconds (AP10). The related curve of the solar input is illustrated by Figure 7.7. After that procedure the salt flow is stopped, no solar radiation arrives the receiver and the closed aperture prevents any heat loss other than the conduction through the receiver walls. The results of this specific shutdown are shown in the diagrams below (Figure 7.8-Figure 7.12). One remarkable result (illustrated by Figure 7.9 and Figure 7.11) is that the salt temperatures are rising for about ten minutes after the valves are closed. The reason for this behavior is that in the current configuration the mirrors need more time to defocus than the valves need to shut. Furthermore, the tubewalls store heat for some period of time, which is slowly delivered to the salt.

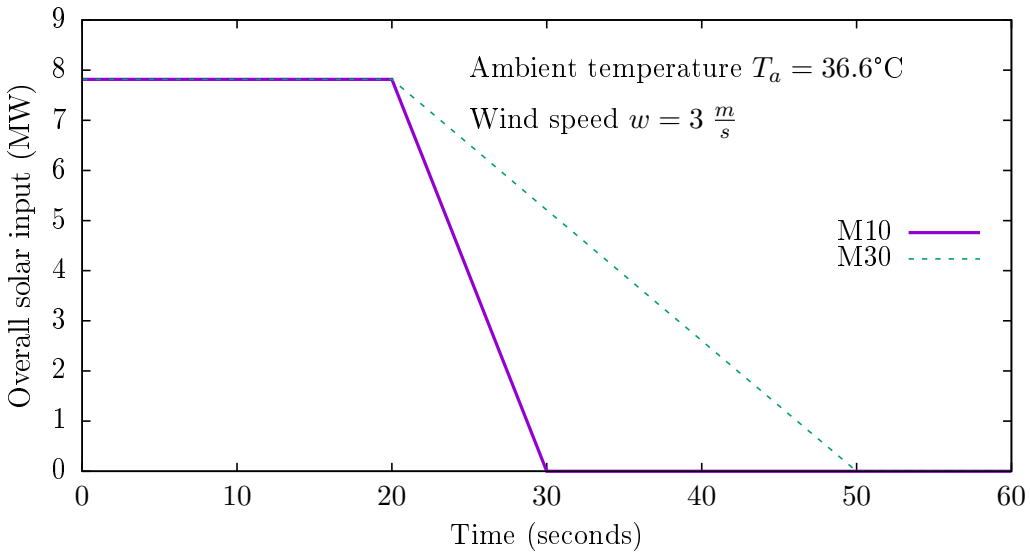

Figure 7.7: Solar input - shutdown M10 or M30

[1]See also subsection 6.3.2

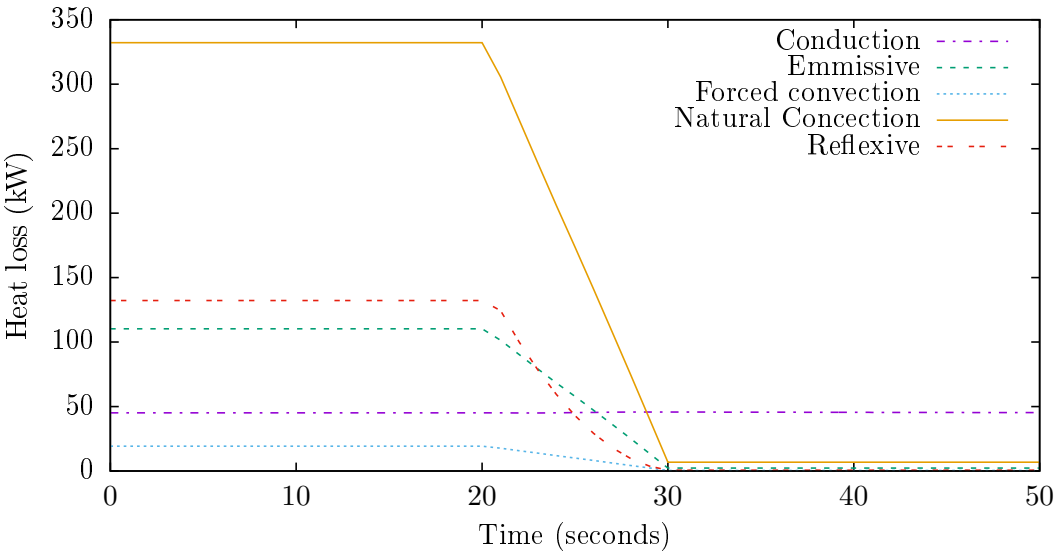

Figure 7.8: Receiver heat losses - shutdown AP10 V5 M10

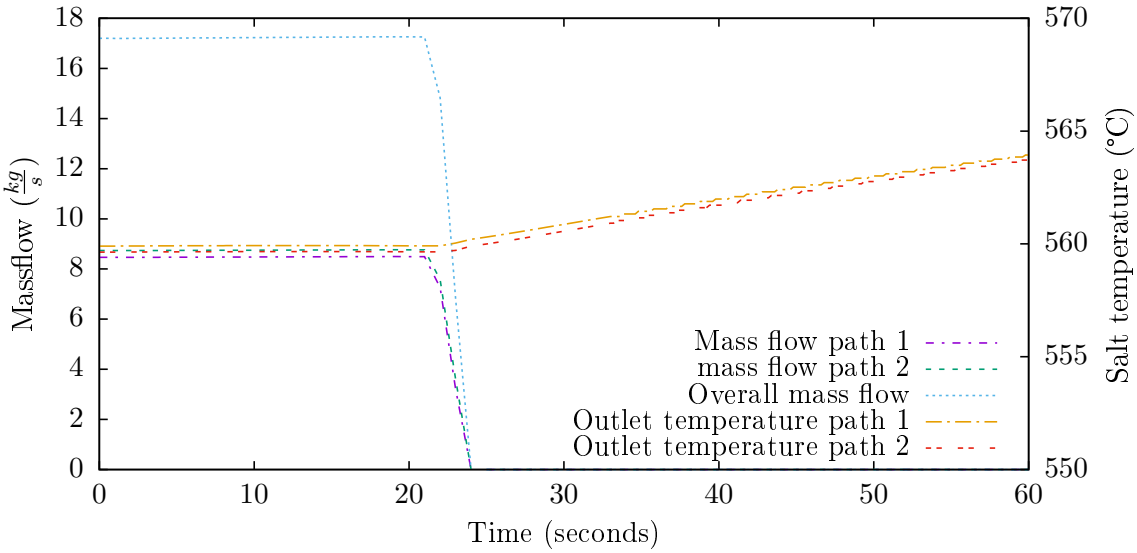

Figure 7.9: The mass flow on the first ordinate is compared to outlet salt-temperatures on the second ordinate - shutdown AP10 V5 M10

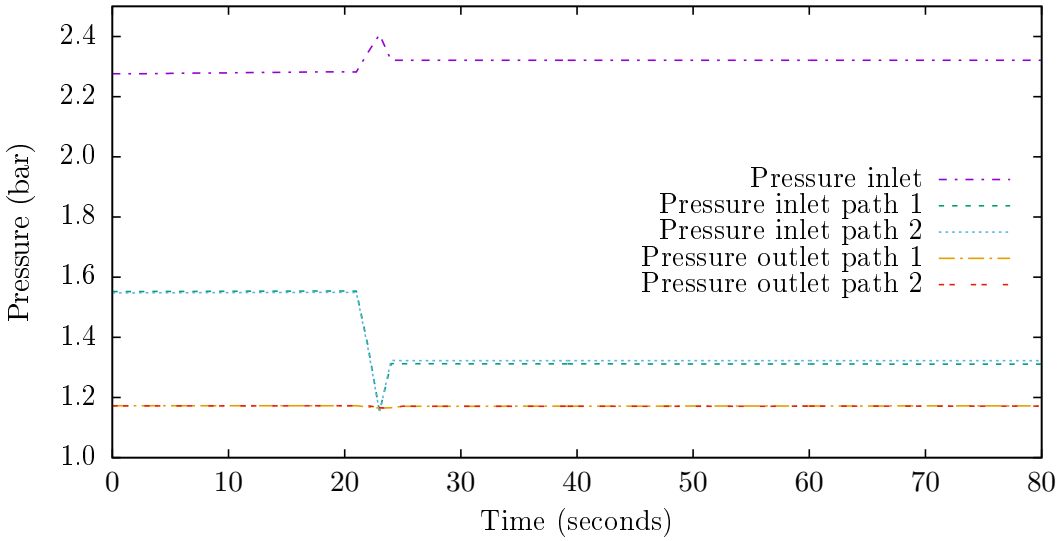

Figure 7.10: Pressures - shutdown AP10 V5 M10

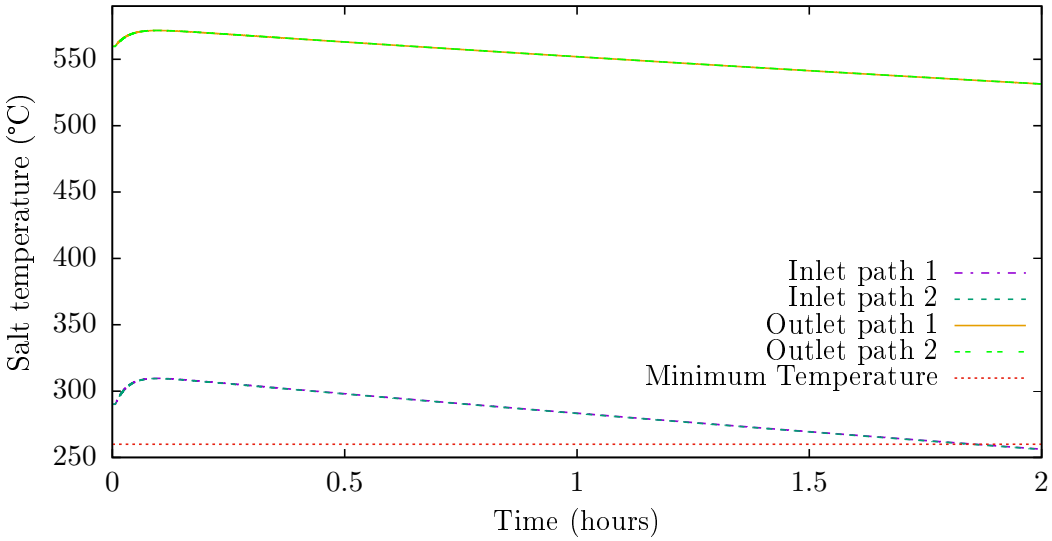

Figure 7.11: Salt temperatures - shutdown AP10 V5 M10

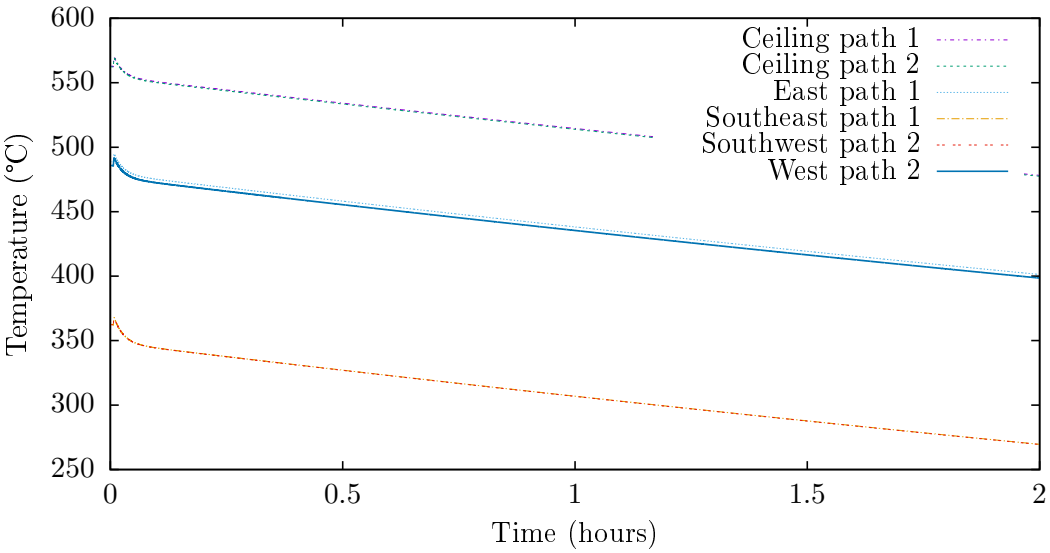

Figure 7.12: Temperatures on the surface of the receiver tubes - shutdown AP10 V5 M10

7.3 Shutdown - APopen V15 M10

In the previous shutdown sequence (section 7.2) the aperture was closed within 10 seconds. Therefore the salt temperature stayed above the minimum temperature for relatively long (nearly 2 hours - Figure 7.11). This means that a "stand by" state **without draining**, as it is realized in this work, seems to be realistic for the used cavity receiver. This results are contradictory to what is recommended in the work by [23], where a design basis for an external receiver is given.[2] It is analyzed if such an "undrained stand by" mode is also possible for a receiver configurations where the aperture could not be closed. One could imagine a situation where the aperture door is stuck or even not installed. The following diagrams (Figure 7.13 - Figure 7.17) show what happens if the control valves are closing within 15 seconds (V15), the mirror defocusing within 10 seconds (M10) and the aperture remains open (APopen). The related curve of the solar input is illustrated by Figure 7.7. It turned out, that the salt temperature reaches critically low levels after about 12 minutes, which means the amount of time before the receiver definitely would have to be either drained or restarted is drastically shortened in comparison to a configuration where the aperture door is shut. Though, the allowed time to remain filled for **external** receivers is given with only one minute [23].

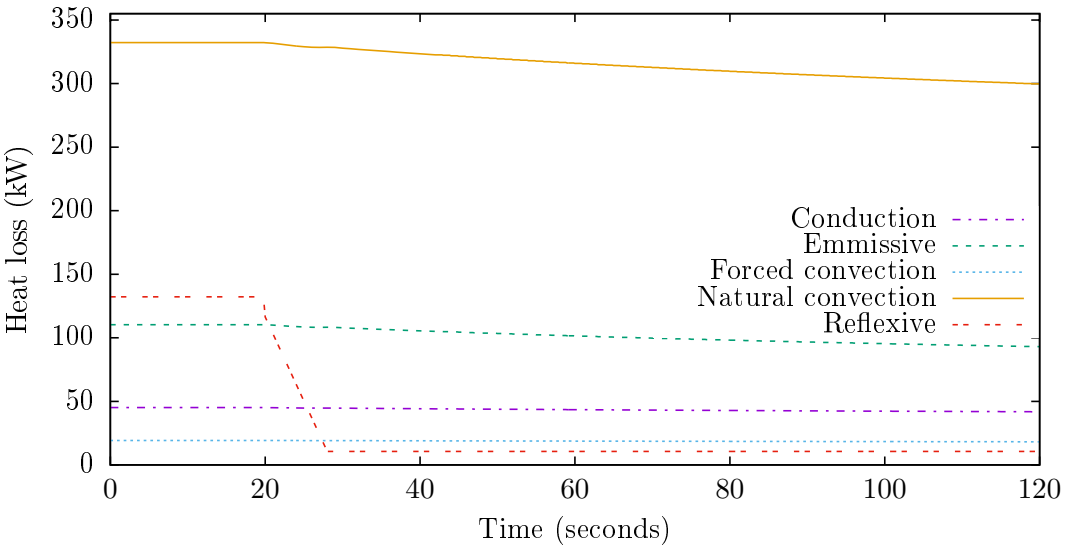

Figure 7.13: Receiver heat losses - shutdown APopen V15 M10

[2]The active tube-walls are attached on the outside of an external receiver. Therefore significantly higher heat losses are expected, which makes it indispensable to drain the receiver very fast in case of a shutdown.

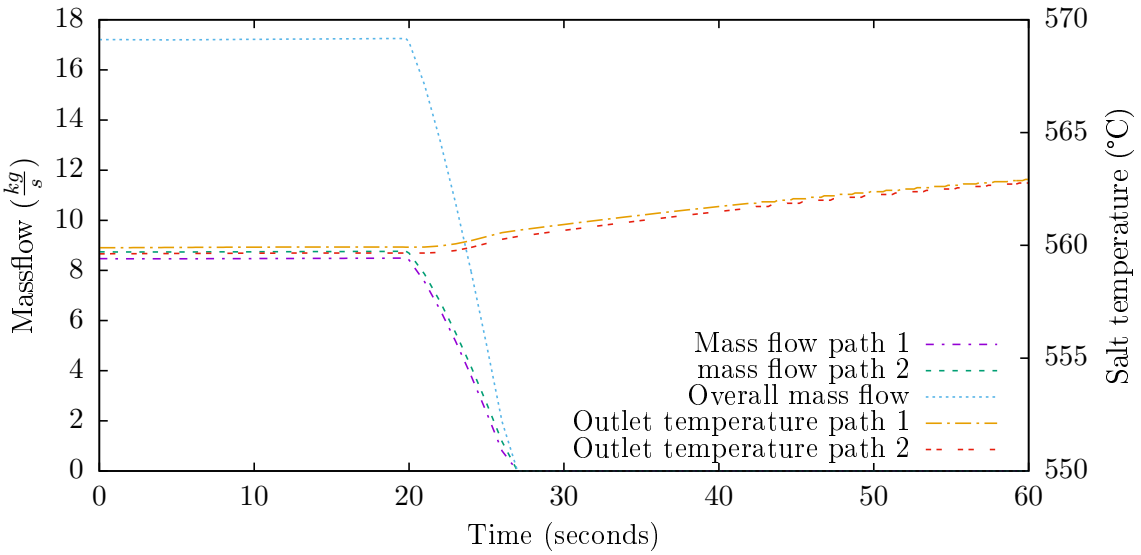

Figure 7.14: The mass flow on the first ordinate is compared to outlet salt-temperatures on the second ordinate - shutdown APopen V15 M10

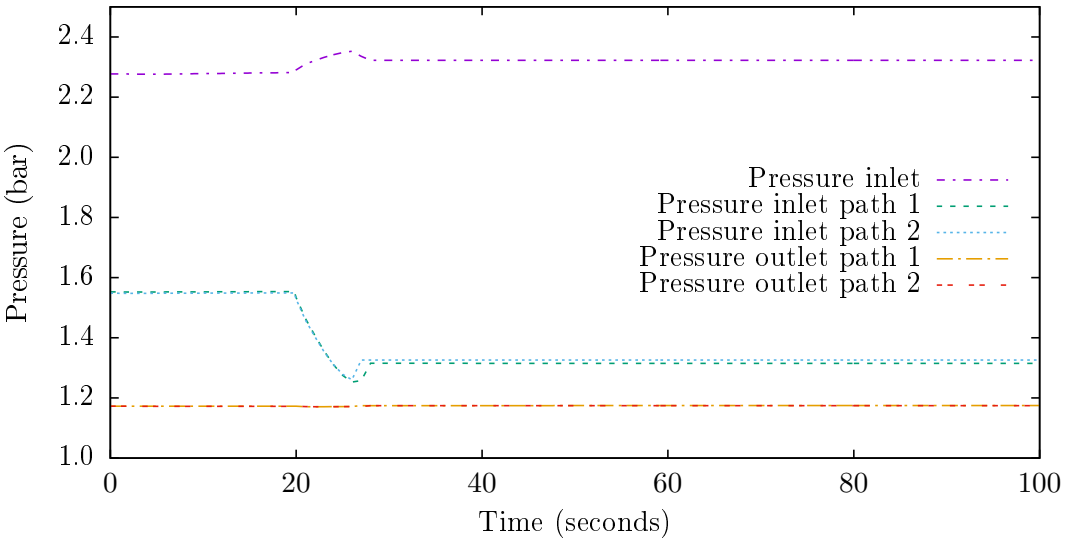

Figure 7.15: Pressures - shutdown APopen V15 M10

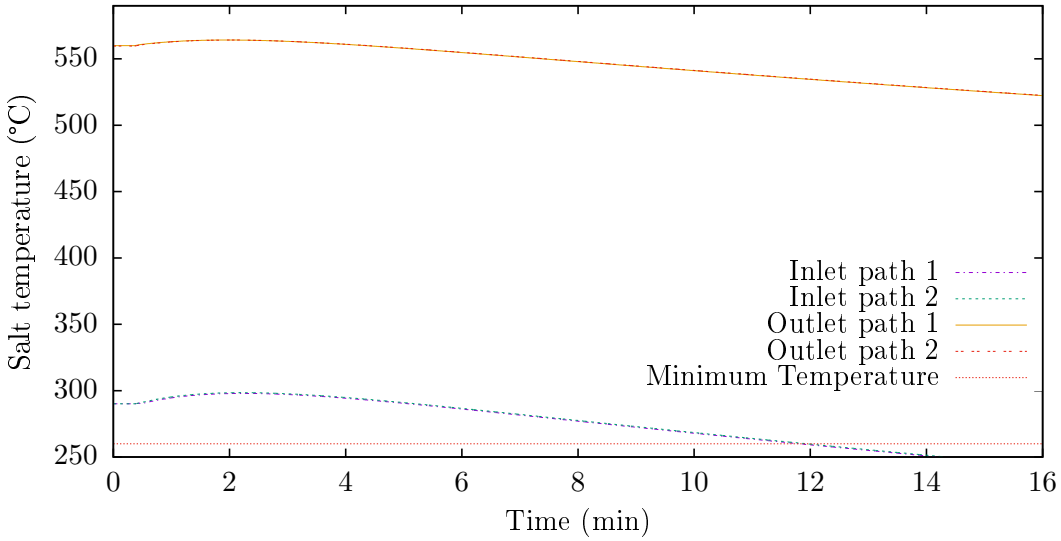

Figure 7.16: Salt temperatures - shutdown APopen V15 M10

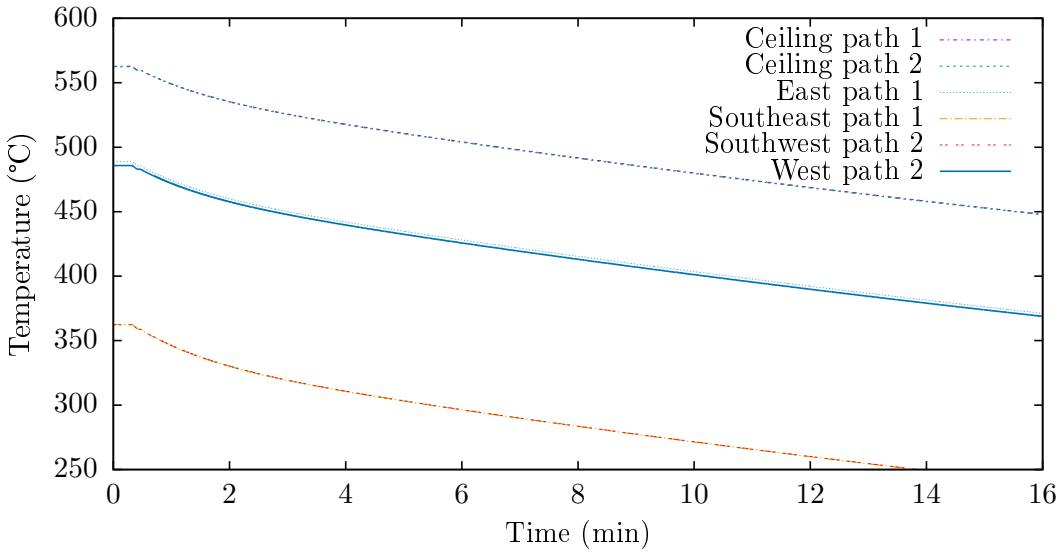

Figure 7.17: Temperatures on the surface of the receiver tubes - shutdown APopen V15 M10

7.4 Comparison of different shut downs

Further specifications, worth looking at, are the variation of the closing time of the aperture, the control valves, or the time, which the mirror field needs to defocus. In reality, depending on the receivers design, some of these parameters could be adjustable in operation, some could be unchangeable. It would be interesting how the "stand by" time could be expanded as long as possible, while also preventing critically high salt temperatures. In this section the influence on the thermal behavior is examined for the variation of the parameters mentioned above. The results are shown in the diagrams below (Figure 7.18- Figure 7.22). Especially Figure 7.20 shows that a faster closure of the valve and a slower defocus sequence lead to significantly higher salt temperatures. The closing time of the aperture obviously has no big influence to the temperature compared to the other parameters, while a major difference in the results is whether or not the aperture is closed at all. The results show that it is beneficial to close the control valve slowly and defocus the mirrors fast to prevent temperature peaks in the salt which could possibly lead to damage. The related curve of the solar input is illustrated by Figure 7.7.

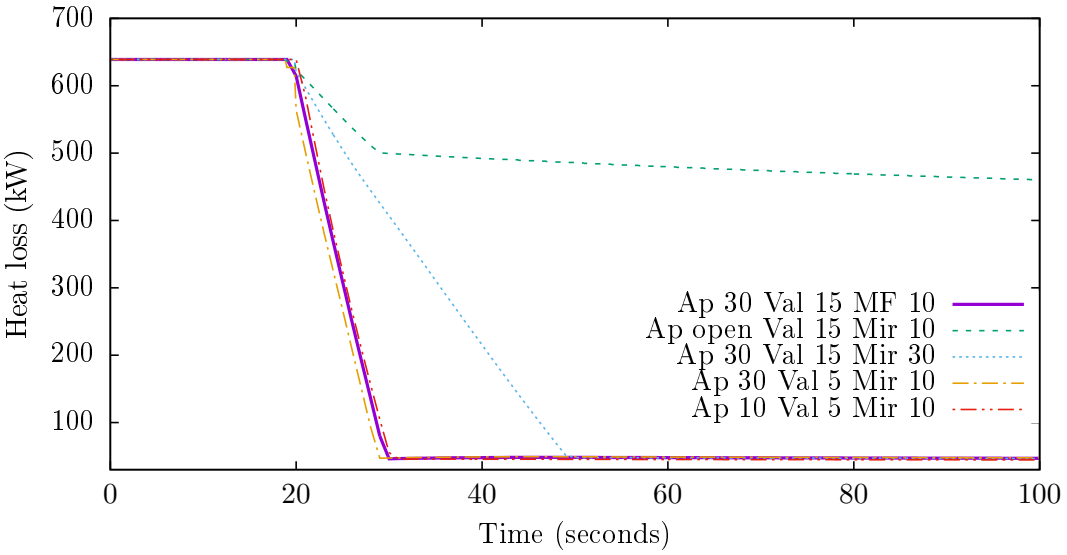

Figure 7.18: Receiver heat losses - different shut downs

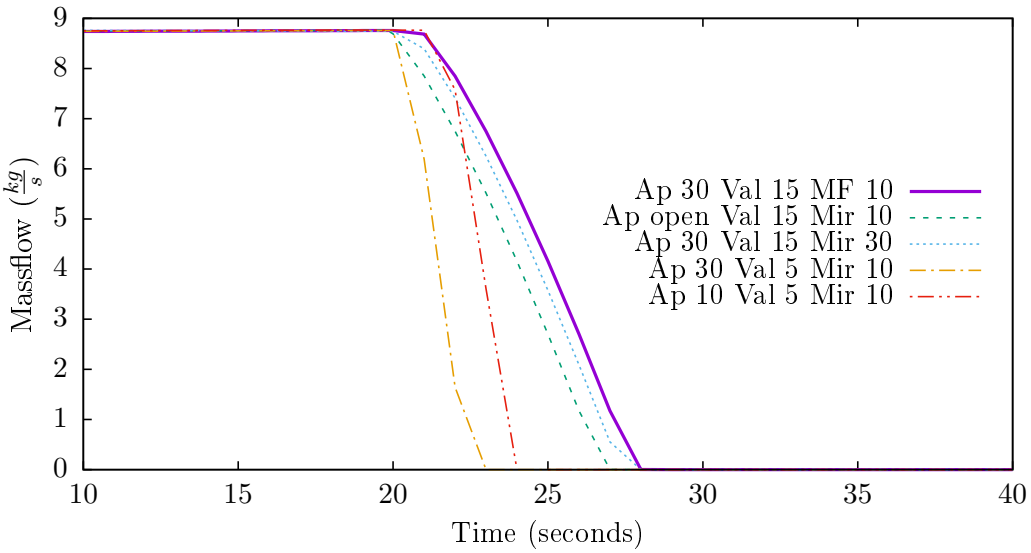

Figure 7.19: Mass flow - different shut downs

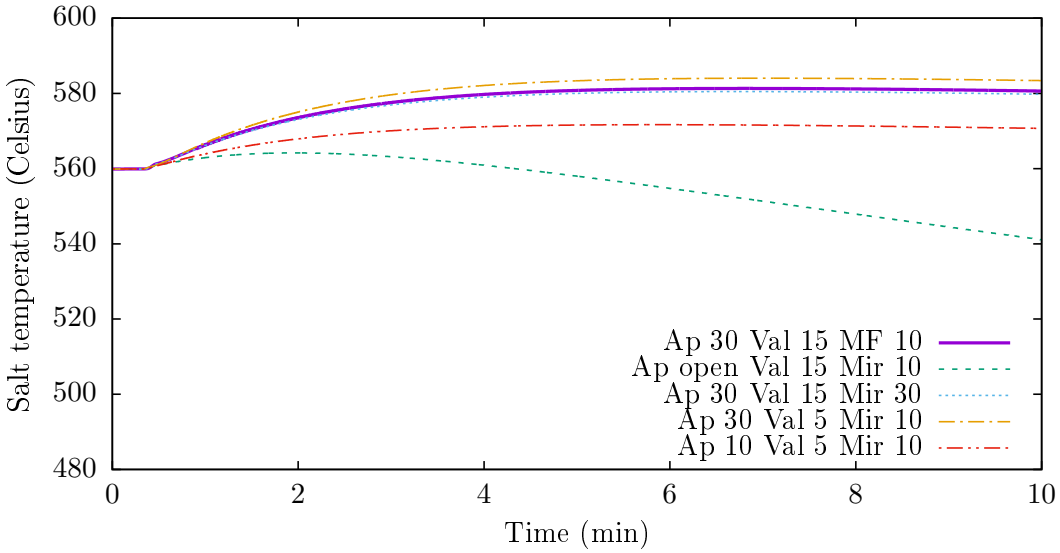

Figure 7.20: Outlet salt temperatures - different shut downs

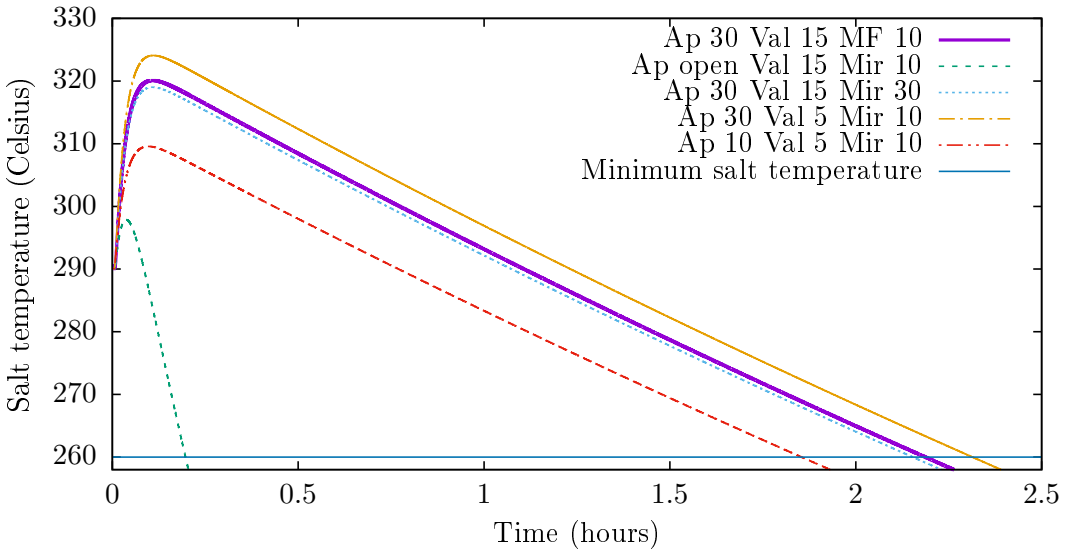

Figure 7.21: Inlet salt temperatures - different shut downs

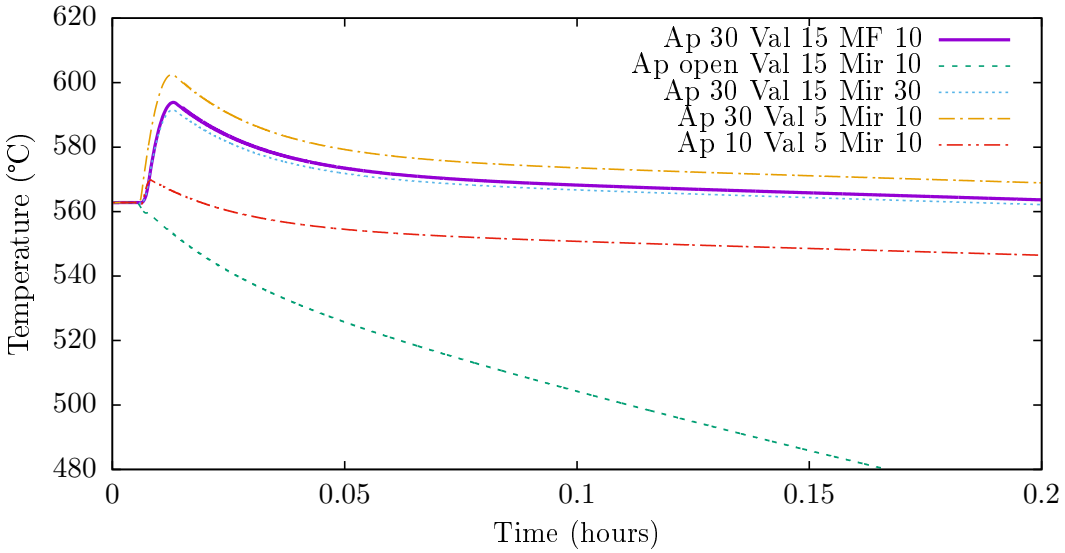

Figure 7.22: Temperatures on the surface of the receiver tubes - different shut downs

7.5 Wholeday

Finally a simulation of the receiver with real weather data was performed to examine the overall behavior. The results are shown in the diagrams of the following section (7.23-7.27). After about 6 hours one can see that a cloud transition takes place and how the controller leads the system to a compensation reaction. The salt cycle is started and shut down automatically once the overall solar input rises above or falls below 1.5 MW. The related curves of the solar input, the wind speed and the ambient temperature are illustrated by Figure 6.1.

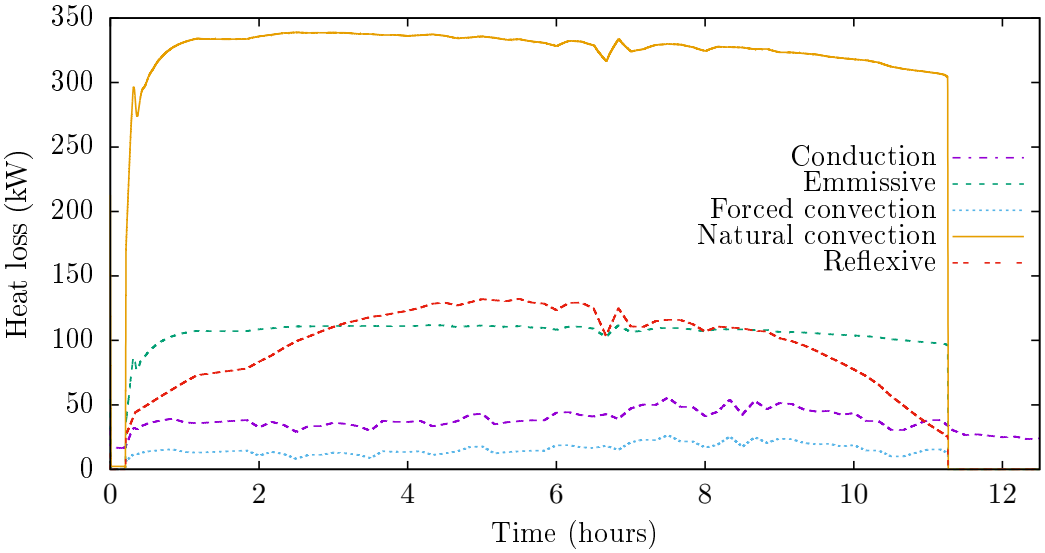

Figure 7.23: Receiver heat losses - wholeday simulation

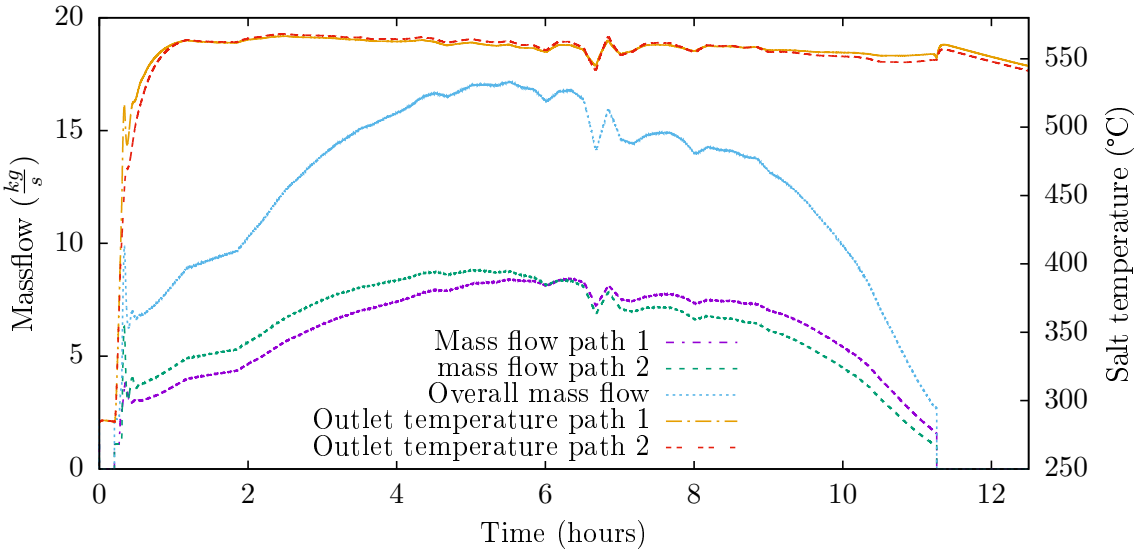

Figure 7.24: The mass flow on the first ordinate is compared to outlet salt-temperatures on the second ordinate - wholeday simulation

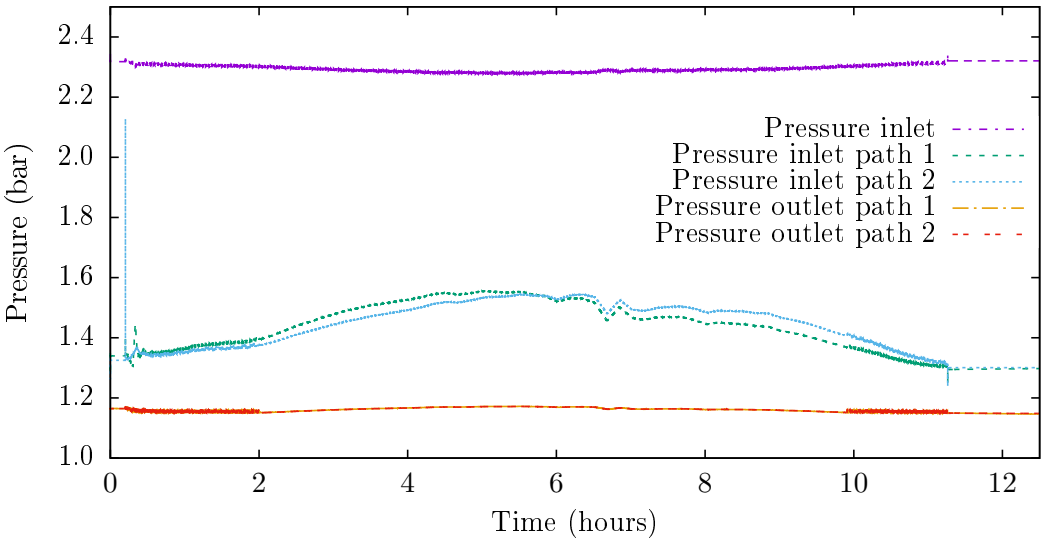

Figure 7.25: Pressures - wholeday simulation

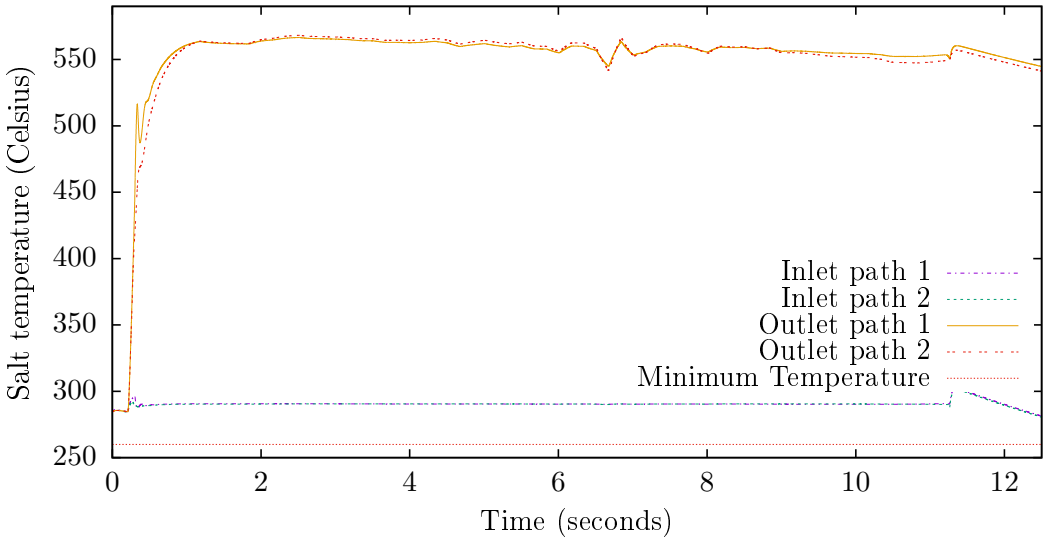

Figure 7.26: Salt temperatures - wholeday simulation

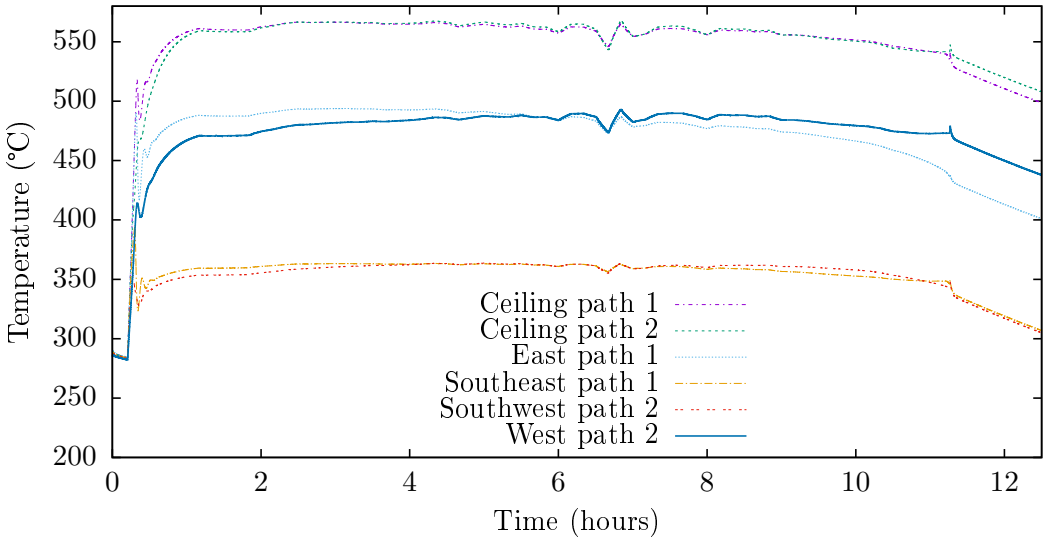

Figure 7.27: Temperatures on the surface of the receiver tubes - wholeday simulation

8 Conclusion

What has been done? The following steps roughly describe the path that has been followed in the current master's thesis to make qualitative statements about the behavior of a solar salt cavity receiver:

- Background literature research.
- Stress and fatigue calculation of a single receiver tube in the scope of a project work.
- Design of the receiver with regard to the given boundary conditions.
- Creation of an APROS model to dynamically simulate the heat transfer fluid "Solar Salt" in the receiver.
- Simulation of different operation transitions for the system, namely the "hot-start", the "shutdown" and the "wholeday" simulation.
- Analysis, editing and visualization of the data sets for the time-dependent properties that were examined.
- Presenting what has been done in form of a diploma thesis.

Interpretation and conclusion of the results Considering the restrictions for the APROS model and the simplifications that were made, the received results are very convincing and informative. It is clear that with the capabilities of the simulation program and the limits of time and manpower, the simulation results cannot be exact, but their interpretation is unambiguous. The curves are of clear and comprehensible shape and the values are plausible and are changing with time as expected.
The results of the hot start simulation show that the salt temperature is the critical parameter because it almost reaches its maximum value (621°C). Therefore the controller has to react fast enough to prevent unbearable high temperature peaks. All other properties remain in a uncritical range and show no high peaks or surprising variation. Also in the "shutdown to stand by" operation transition, the salt temperatures (measured at the inlets of the receiver paths) are the only critical variables. In this case it is only allowed to stay in the "stand by" mode until the salt temperature at any point falls below the crystallization point (238°). To keep some safety margin to that point, the

minimum operation temperature is chosen with 260°C [23]. This simulation shows, that in contrast to the recommended draining of the receiver in case of "stand by" mode for external receivers (See also [23]), it should be possible to let the salt reside inside the current **cavity** receiver. This would be a huge advantage of cavity receivers with closeable aperture doors compared to others. The results of the heat loss calculation show that the losses of the forced convection due to the wind are quite low compared to the natural convection. In contrast to the cavity receiver, the influence of the wind on the heat losses is not that high as it would be for an external receiver. By comparing the different shut downs, shown in section 7.4, a few very interesting statements about the receiver could be made. Firstly, the possibility to close the apertures increases the amount of time that the system is allowed to remain filled in the "stand by" mode, but even without the closure of the aperture it should be possible to remain undrained for a relatively short period of time ($<$ 12 minutes[1]). Furthermore the closing time of the control valves and the time needed to defocus the mirrors, are very important parameters to prevent problematically high temperature peaks of the salt. Last but not least the closing time of the aperture does not have a very high influence on the salt temperatures compared to the other parameters if we stay in a time range of a few minutes (closing or defocusing time). The "wholeday" simulation is a good way to check the overall functionality of the receiver and the control system. The results show that the model was implemented the right way and the receiver can easily compensate cloud transitions lasting up to half an hour without going into "stand by".

Future tasks The most important required future improvement, to make the result even more convincing, is to find a way to simulate the draining of the solar salt system. This is an extremely important feature of solar power plants due to sunlight being unavailable at night and the danger of crystallization of the salt. To realize this simulation, a new model could be build with another simulation program or the existing model could be improved with APROS, but one would have to wait for the new version of the software with new appropriate features. Finally, the results of the simulation and especially the heat loss model, have to be proven by empirical experiments on model power plants.

[1]See also Figure 7.16

A Apendix - APROS process and automation diagrams

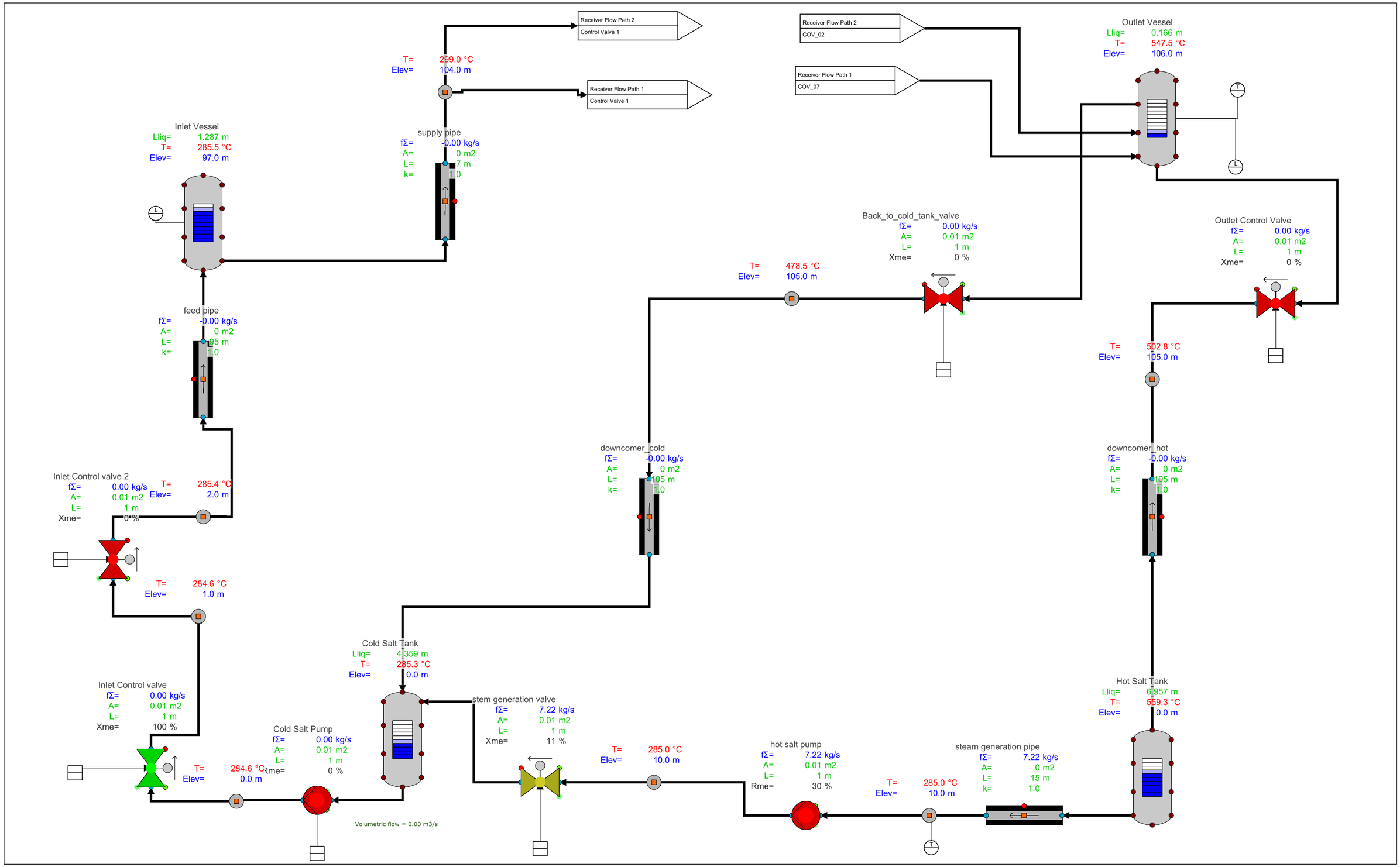

Figure A.1: Basic cycle

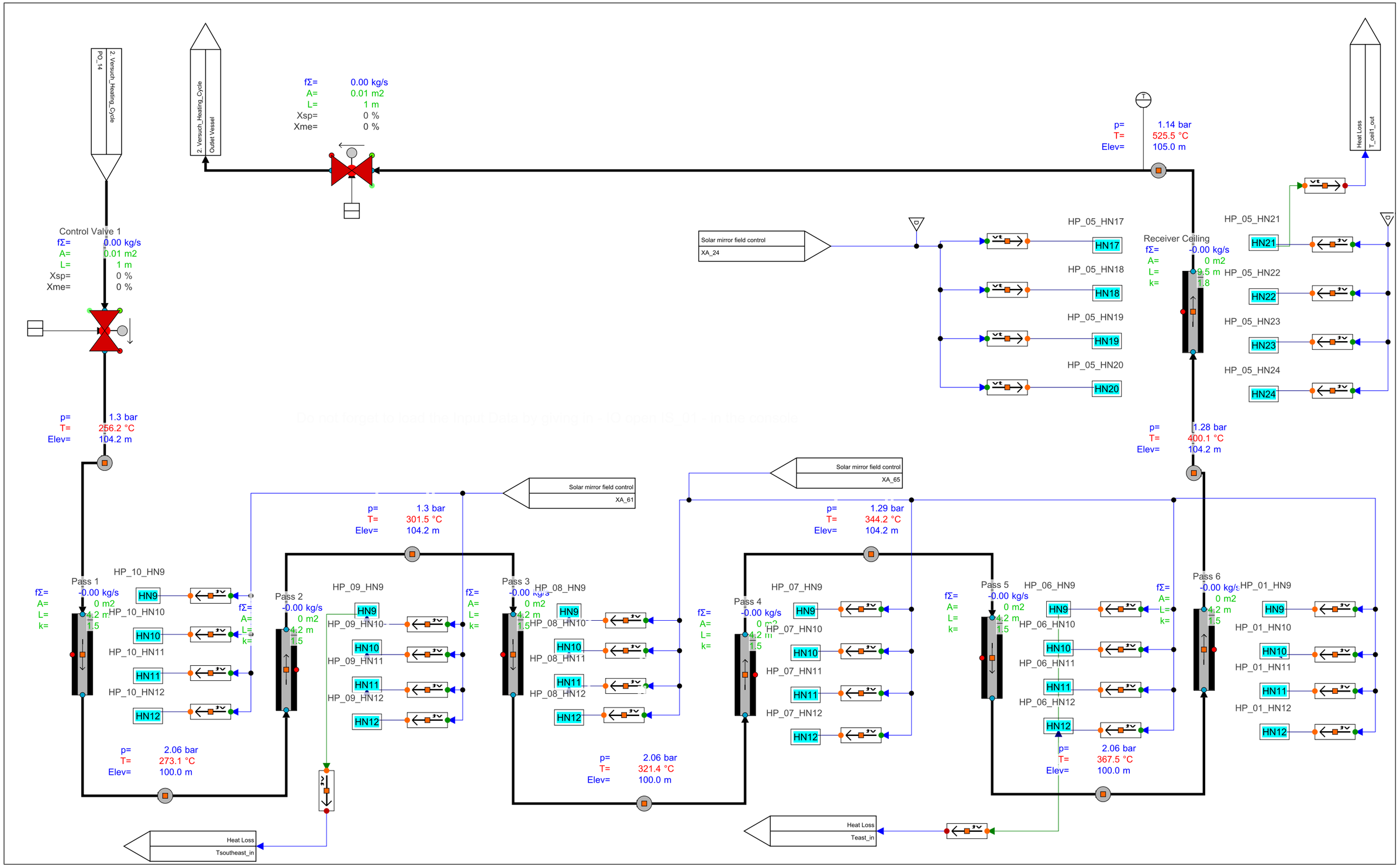

Figure A.2: Flow path 1

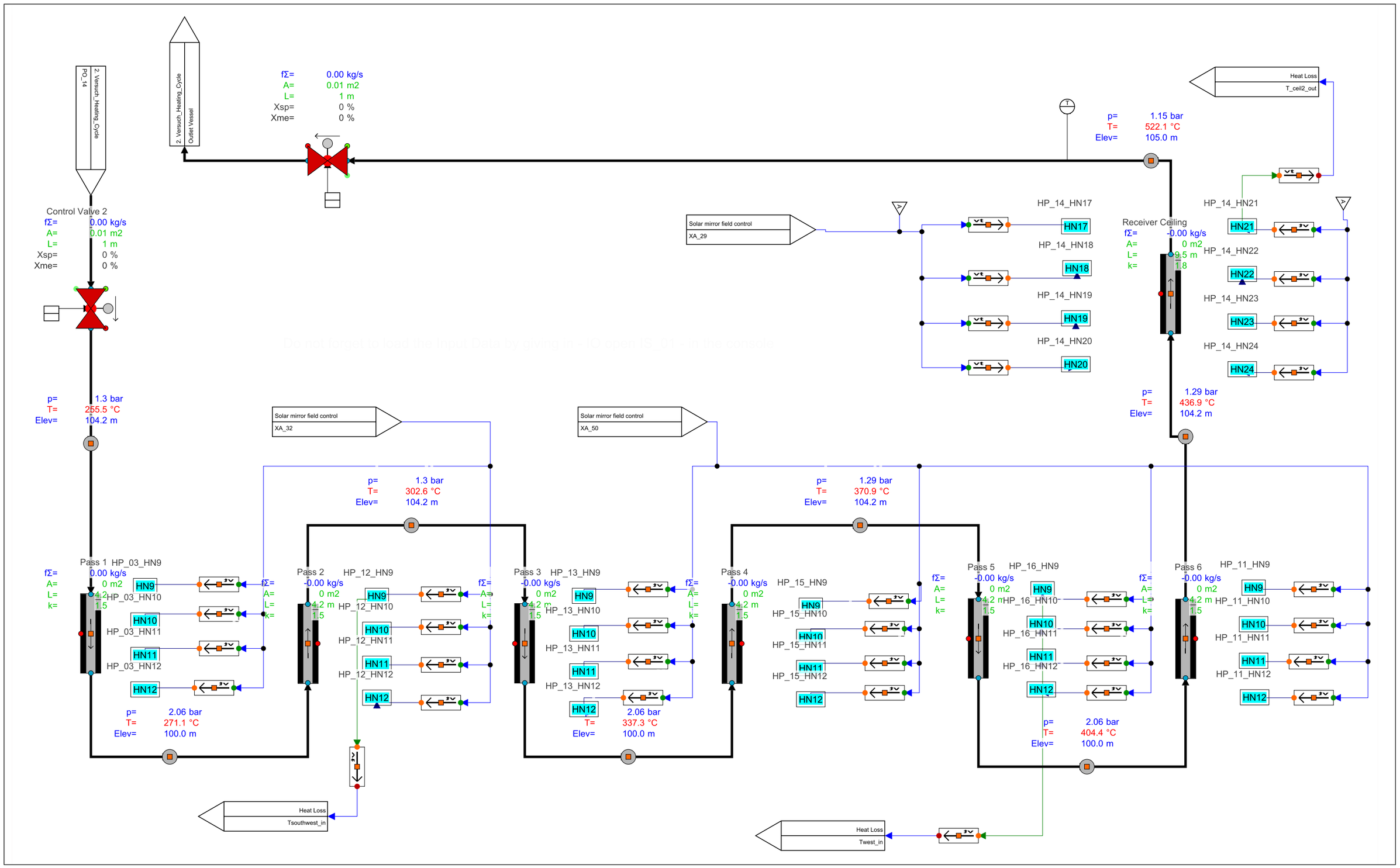

Figure A.3: Flow path 2

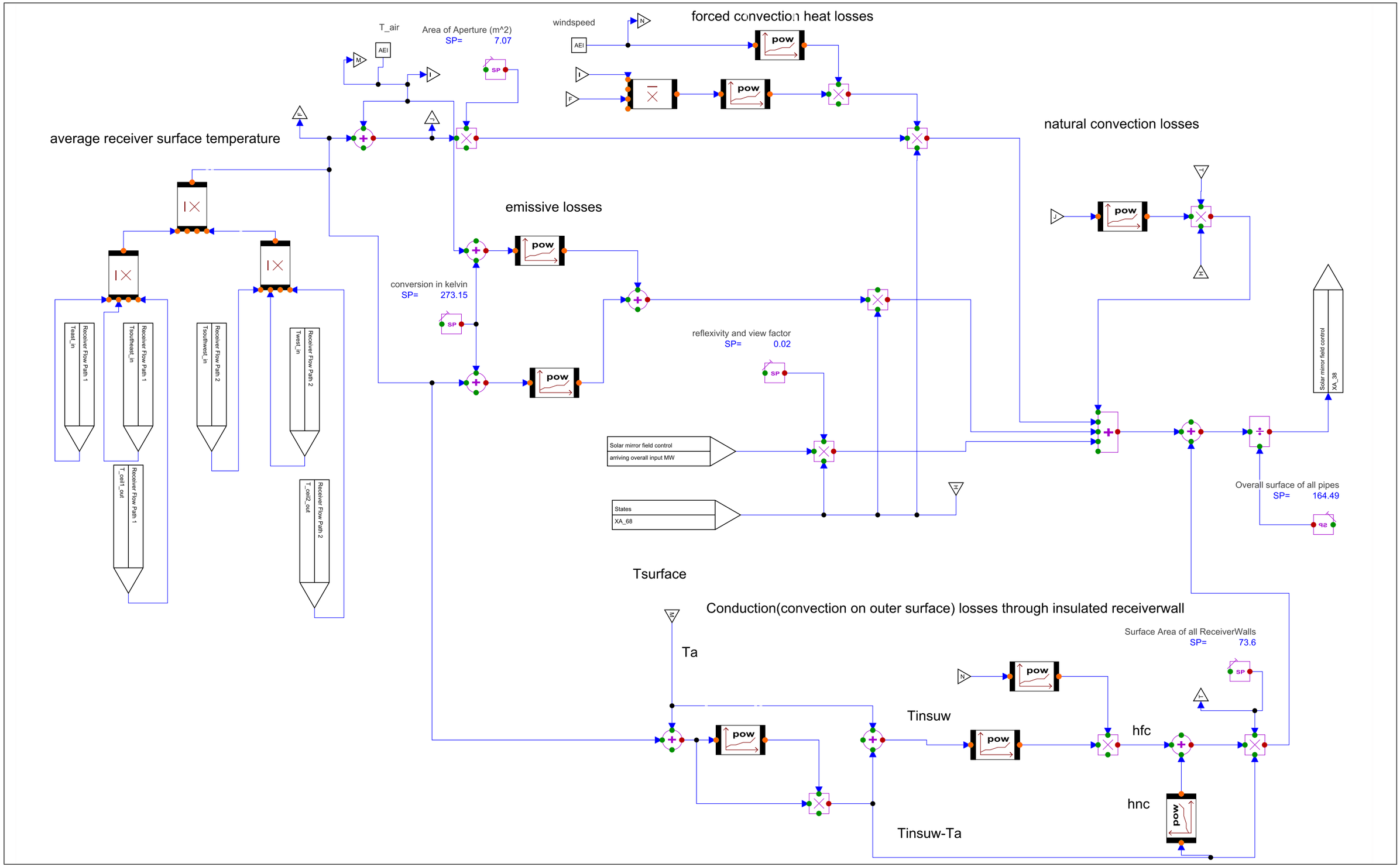

Figure A.4: Heat loss control

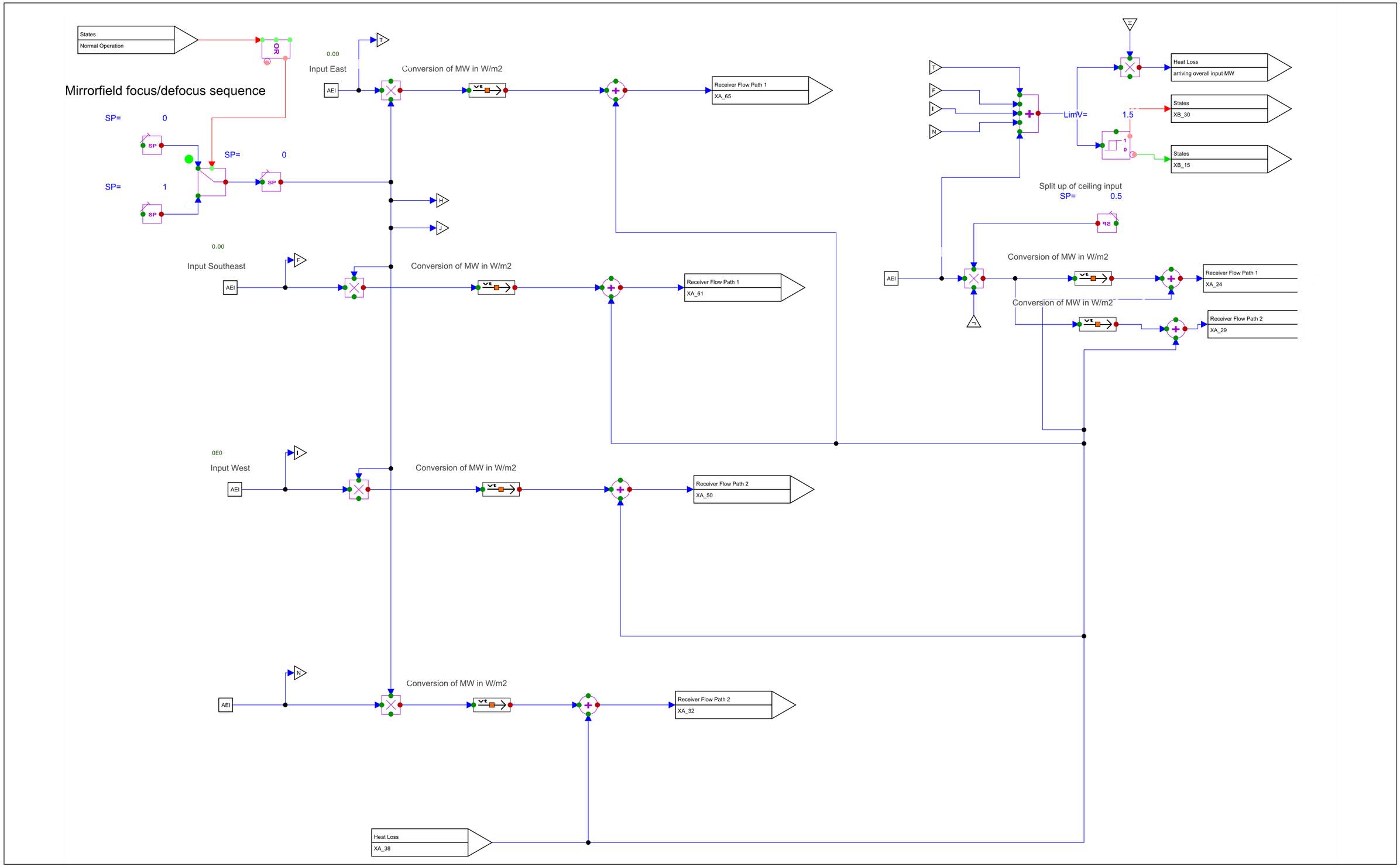

Figure A.5: Mirror field control

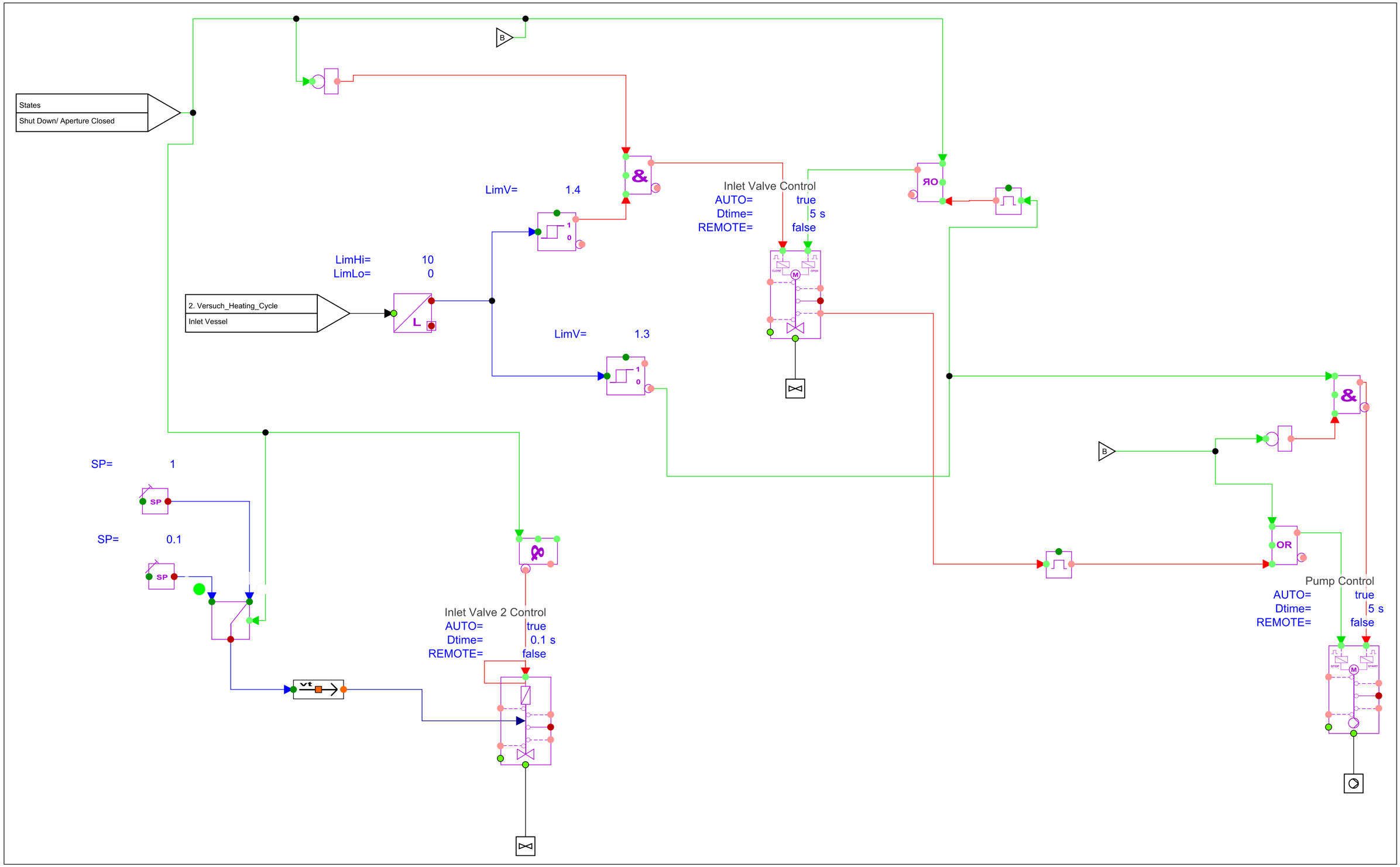

Figure A.6: Inlet tank control

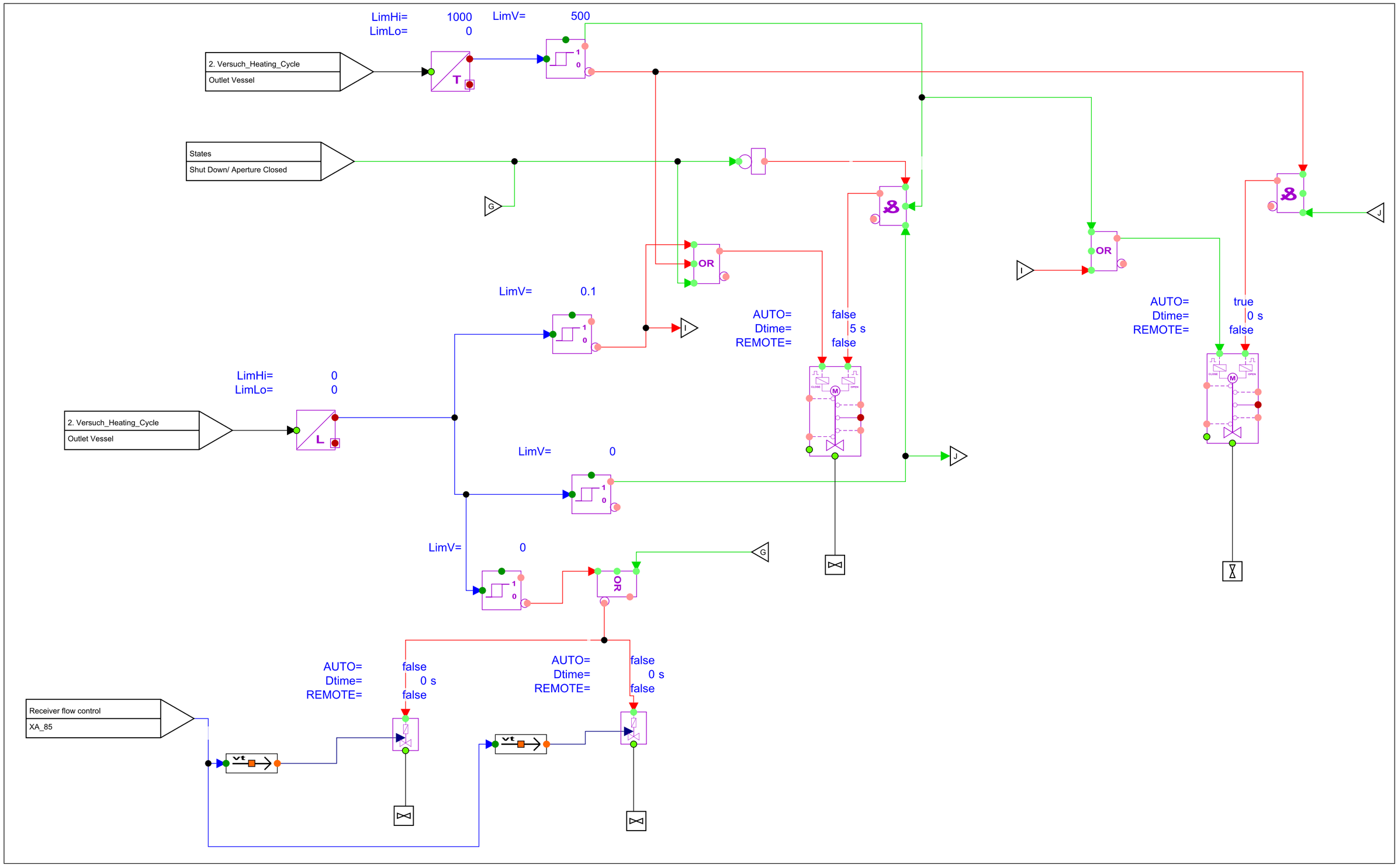

Figure A.7: Outlet tank control

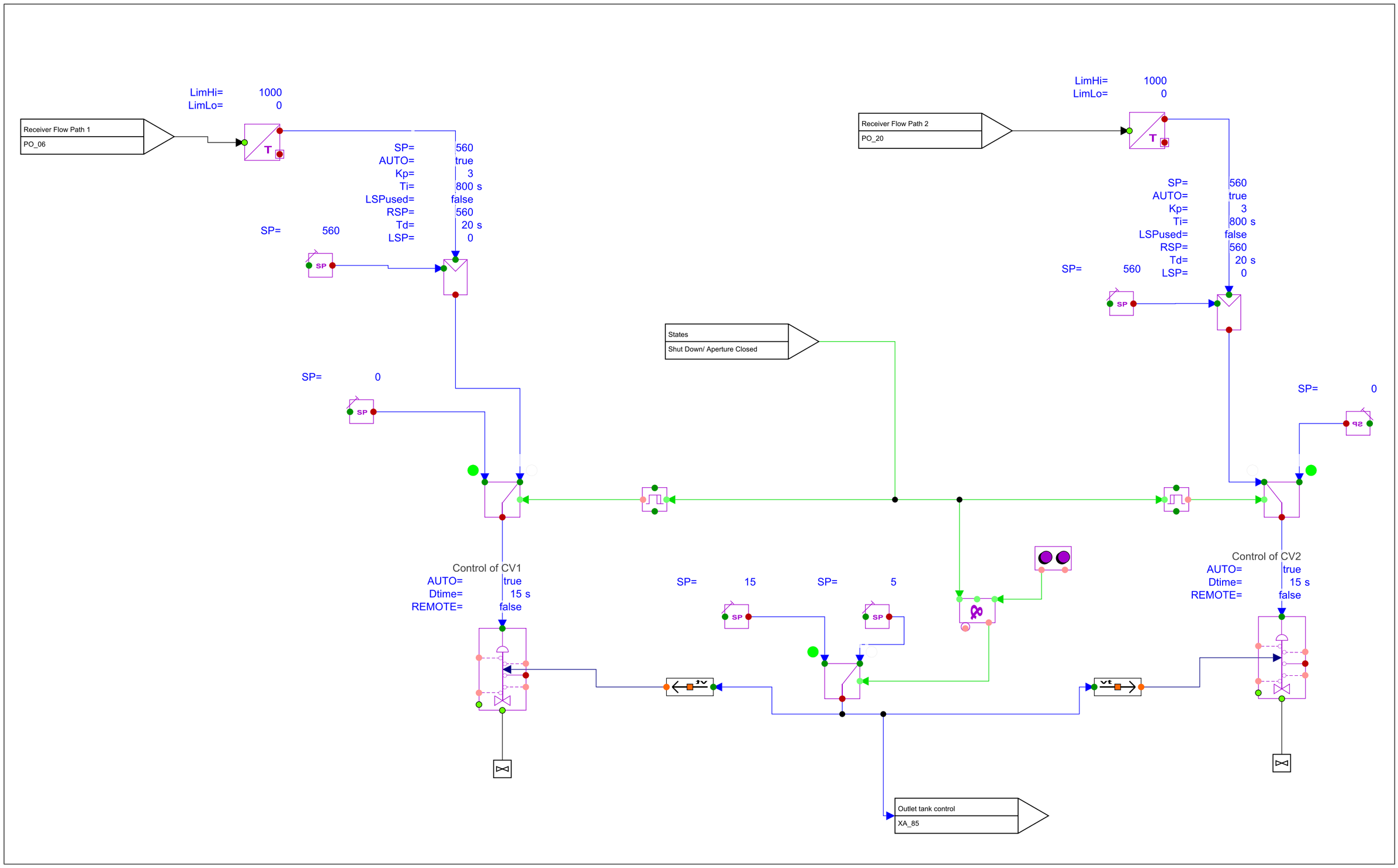

Figure A.8: Receiver flow control

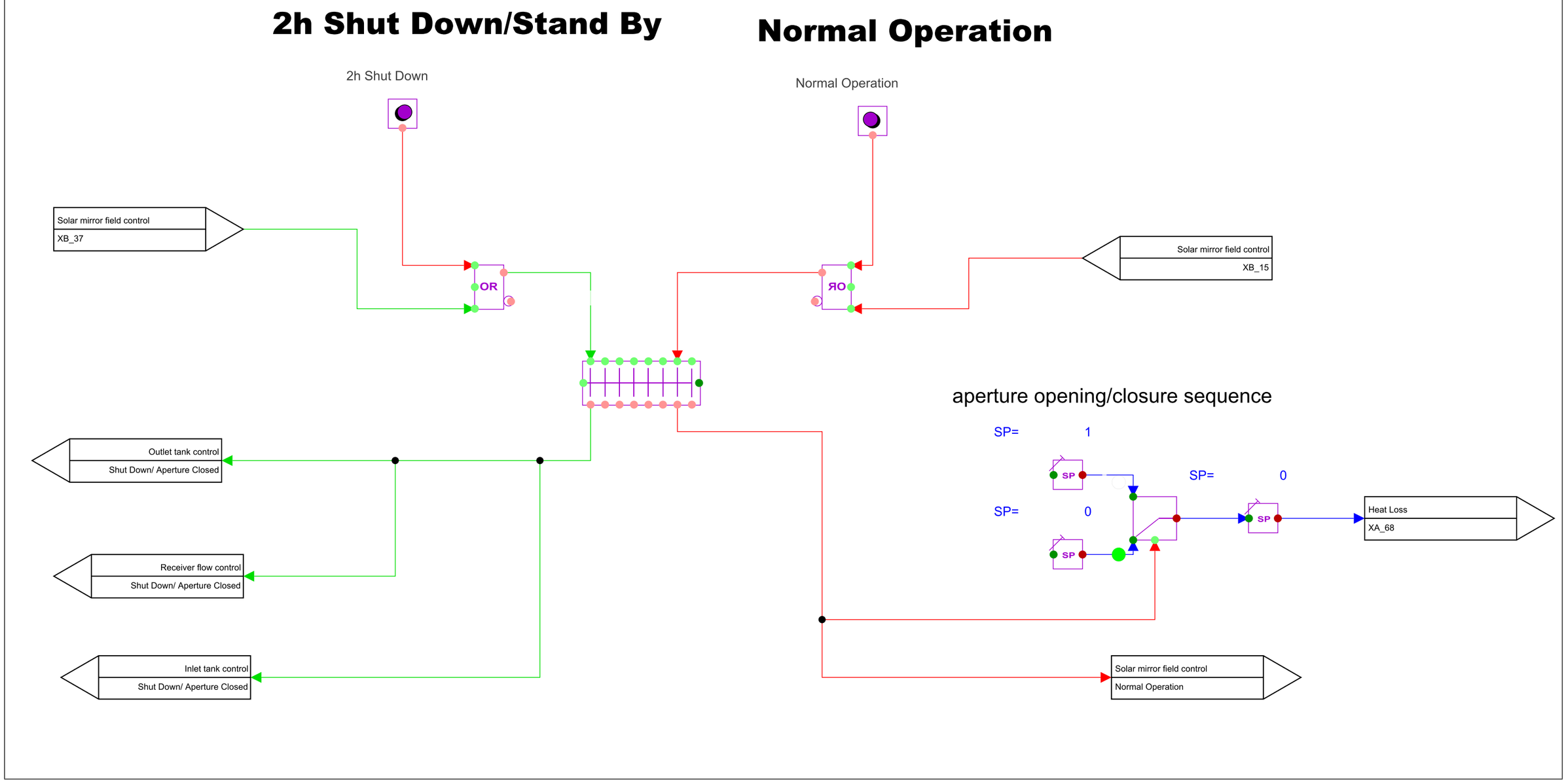

Figure A.9: State control

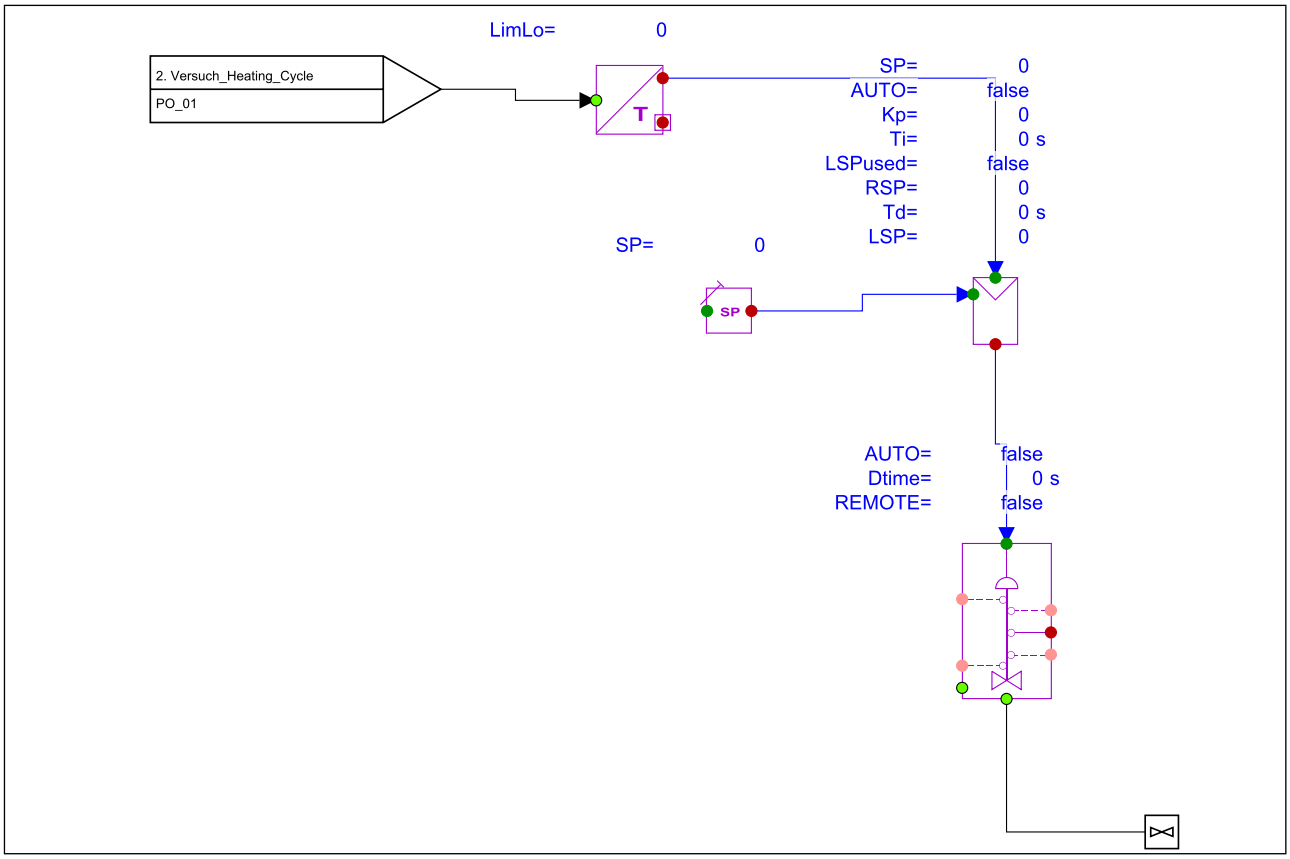

Figure A.10: Steam generation flow control

Bibliography

[1] APROS 6.03 Software documentation.

[2] Information about gemasolar plant - booklet. http://www.torresolenergy.com/TORRESOL. Torresol Energy.

[3] Jamuba Weather Data Pvis on sections V01 FG 14508. Excel data sheet provided by STT Germany and handed over by Philip Schadauer.

[4] *Temperatur in Membranwänden bei einseitiger Beheizung durch Strahlung.* Internal document IET.

[5] *DIN, EN 10088-3: Nichtrostende Stähle–Teil 3: Technische Lieferbedingungen für Halbzeug, Stäbe, Walzdraht, gezogenen Draht, Profile und Blankstahlerzeugnisse aus korrosionsbeständigen Stählen für die allgemeine Verwendung.* Normenausschuss Eisen und Stahl (FES) im DIN, 2011.

[6] *DIN EN 12952-3: Wasserrohrkessel und Anlagenkomponenten –Teil 3: Konstruktion und Berechnung für drucktragende Kesselteile.* Normenausschuss Rohrleitungen und Dampfkesselanlagen (NARD) im DIN, 2011.

[7] Technology Roadmap, 2014.

[8] R. Abdiwe. Investigations on convection heat loss from solar tower receivers with different wind speed conditions, 2013. Institute for Energy Systems and Thermodynamics.

[9] Andrea Ambrosini Marlene Bencomo Aaron Hall Clifford K. Ho, A. Roderick Mahoney and Timothy N. Lambert. Characterization of pyromark 2500 for high-temperature solar receivers. Proceedings of ASME 2012 6th International Conference on Energy Sustainability 10th & Fuel Cell Science, Engineering and Technology Conference ESFuelCell2012, July 2012. San Diego, CA, USA.

[10] AK Das, P Iñigo, RJ Terdalkar, A Joshi, C Wang, MM Clark, D McGrane, and L Deng. Design features and control concepts of alstom molten salt receiver. *Energy Procedia*, 69:350–359, 2015.

[11] VDI e. V. Vdi-wärmeatlas, 2013.

[12] Joseph H Faupel. *Engineering Design; a Synthesis of Stress Analysis and Materials Egineering.* J. Wiley, 1964.

[13] Fortum and VTT. *Thermal Hydraulics - APROS.* Course material provided by VTT/Fortum.

[14] Markus Haider. Skritptum Angewandte Thermodynamik, October 2010.

[15] Xin Li, Weiqiang Kong, Zhifeng Wang, Chun Chang, and Fengwu Bai. Thermal model and thermodynamic performance of molten salt cavity receiver. *Renewable Energy*, 35(5):981–988, 2010.

[16] Peter Marks. *Amerikanische Stahlsorten: Leitfaden für den Vergleich amerikanischer Stahlsorten mit EN-bzw. DIN-Normen Deutsch/Englisch.* Beuth Verlag, 2012.

[17] Lukas Panzer. Temperaturverteilung, Spannungsverteilung und Ermüdungsberechnung in strahlungsbeheizten, „Solar Salt“ gekühlten Membran- und Einzelrohrwänden. Wien, Techn. Univ., Proj.-Arb., 2015.

[18] Rudolf Pich. *Theoretische Untersuchung der Temperaturverteilung in strahlungsbeheizten Kesselrohren.* EVT, Energie-u. Verfahrenstechnik GmbH, 1973.

[19] Philip Schadauer. Dynamic simulation of a solar tower receiver. Master's thesis, 2015. Wien, Techn. Univ., Dipl.-Arb.

[20] Dennis L Siebers and John S Kraabel. Estimating convective energy losses from solar central receivers. Technical report, Sandia National Labs., Livermore, CA (USA), 1984.

[21] Thomas Steinparzer. Off-gas heat recovery for steelmaking processes based on thermal energy storage, 2014. Parallelt. [Übers. des Autors] Wärmerückgewinnung aus dem Heißgas der Stahlerzeugung unter Einsatz von Wärmespeichern; Wien, Techn. Univ., Diss., 2014.

[22] U Witte. *Steinmüller: pocket book: steam generation.* Vulkan-Verlag, 2nd english edition edition, 1994.

[23] Alexis B Zavoico. Design basis document. *Sandia National Laboratories, SAND2001-2100, Albuquerque, NM*, 2001.